https://doi.org/10.5194/egusphere-2025-3269
Preprint. Discussion started: 29 September 2025

Evidence and interpretation of non-linear recession behaviour in a periglacial cliff at Port Foster, Deception Island (South Shetlands, Antarctica).

Carlos Paredes[1], Inés Santalices[1], Celia Sanchíz[2], Miguel Angel Ropero[3,1]

[1]Dpt. Geological and Mining Engineering, School of Mines and Energy, Universidad Politécnica de Madrid. Rios Rosas 21, 28003 Madrid, Spain
[2]Laboratorio de Ingenieros del Ejército "General Marvá". LABINGE. Instituto Nacional de Técnica Aeroespacial (INTA). Princesa 38, 28008 Madrid, Spain.
[3]Escuela Politécnica Superior del Ejército de Tierra (ESPOL), Ministerio de Defensa, Joaquín Costa 6, 28002 Madrid, Spain.

Correspondence to: Carlos Paredes (carlos.paredes@upm.es)

Abstract.

Cliff recession in periglacial coastal environments is highly sensitive to climate-driven changes in temperature, sea ice, and permafrost dynamics. While previous studies have predominantly relied on linear models to describe shoreline retreat, these methods often fail to capture the non-linear, episodic, and threshold-driven nature of coastal erosion in cold regions. Moreover, the scarcity of high-resolution, long-term datasets in polar regions, particularly in Antarctica, has limited the development of predictive models tailored to these dynamic systems. This study aims to improve the understanding of long-term cliff recession patterns in periglacial environments by applying advanced non-linear statistical modelling to a multitemporal dataset. Focusing on the coastal bluffs of Port Foster, Deception Island (South Shetlands, Antarctica), we examined geomorphological changes over a 66-year period (1956–2022), using a unique combination of historical aerial photographs and high-resolution satellite imagery. Photogrammetric pre-processing, orthorectification, and manual digitisation of reference lines were integrated into a transect-based statistical analysis framework. The study applied both linear and non-linear least squares regression models—quadratic and sigmoidal—to reconstruct spatial-temporal erosion trends, with uncertainty-weighted parameters incorporated into the estimation. Results reveal a distinct shift from quasi-stable to accelerated recession after 2000, particularly in areas exposed to dominant marine and thermal forcing. Linear models underestimated these trends, while sigmoidal logistic models more accurately identified inflection points in erosion rates. Maximum recession rates reached up to 5 m/year in the central bluff segment. The findings underscore the importance of integrating non-linear modelling into coastal monitoring and management frameworks, especially in vulnerable and data-scarce polar environments. This approach provides a more realistic understanding of periglacial coastal dynamics and highlights the critical need for adaptive strategies to address climate-induced instability near strategic infrastructure such as research stations.

1 Introduction

The dynamic of polar coastlines is governed by a complex interplay of sea, ice, permafrost, and soil. These systems are highly sensitive to climatic warming, particularly in the Arctic and Antarctic regions, where the most visible impact is coastal retreat due to accelerated erosion processes (Irrgang et al., 2022; Liew et al., 2022; Aga et al., 2024;). Although less frequent, shoreline progradation also contributes to coastal evolution. Coastal change is driven by interacting oceanographic, terrestrial, periglacial, and paraglacial processes that modulate shoreline position and sediment transport, influencing nutrient, carbon, and pollutant fluxes across nearshore zones. Coasts underlain by permafrost are especially vulnerable to temperature increases. Air warming accelerates thawing both from the surface and laterally through exposed cliff faces, increasing their susceptibility to mass wasting and sediment loss (Li et al., 2023; Wang et al., 2023). These transformations are expected to intensify under continued warming, exacerbated by declining sea ice extent and rising sea levels (Barnhart et al., 2014b; Bamber et al., 2019; Sun et al., 2023; Gilbert and Holmes, 2024). Quantitative assessments of these changes are essential for anticipating future erosion trajectories and for informing adaptation strategies in polar environments.

Globally, around 52% of shorelines comprise cliffs, bluffs, coastal escarpments and other steep landforms (Young and Carilli, 2019). These abrupt coastal systems are shaped by a variety of interdependent processes—marine, subaerial, and anthropogenic—often exhibiting spatial and temporal variability in erosion patterns (Sunamura, 1992, 2015; Davidson, 2021). Where sediments are fine-grained or poorly consolidated, retreat is typically more pronounced and less predictable. These coastal environments are subject to highly complex erosion processes, particularly where softer materials dominate (Prémaillon et al., 2018). In such settings, sediment supply is mediated by fluvial and estuarine contributions and conditioned by geological structure. Wave and tidal parameters modulate sediment redistribution, while sea-level rise and increased storm intensity are expected to heighten erosion risks in the coming decades (Nicholls and Cazenave, 2010; Griggs and Reguero, 2021). As a result, coastal cliff retreat rates are expected to intensify, complicating future predictions (Trenhaile, 2011; Limber et al., 2018; Matsumoto et al., 2024). These changes pose significant challenges for long-term prediction and necessitate precise tools for monitoring, evaluating and modelling coastal response (Balaji et al., 2017; Schoonees et al., 2019).

In this context, understanding both past and present shoreline behaviour becomes vital for coastal management, allowing for site-specific adaptation strategies (Burningham and Fernandez-Nunez, 2020). The seminal work of Tanner (1978) presents a framework for quantifying spatio-temporal variations in coastal position and has become a cornerstone methodology, the Shoreline Change Analysis (SCA) for assessing erosion trends and informing management. While numerous tools and techniques exist to implement SCA, their effectiveness hinges on the availability of long, continuous datasets and the suitability of statistical models for representing complex shoreline dynamics. SCA employs transect-based methods (TBM), where shoreline positions intersect a series of transects anchored to a baseline, facilitating the evaluation of forecasting techniques (Dolan et al., 1978; Srivastava, 2005). TBM-based tools require GIS integration for data processing and analysis. Examples include BeachTools (Zarillo et al., 2008), SCARPS (Jackson, 2004), and DSAS (Danforth and Thieler, 1992), which has been an ArcGIS extension since 1992. The latest standalone version (Himmelstoss et al., 2024) eliminates the need for database import/export. Open-source alternatives such as ODSAS (Gómez-Pazo et al., 2022) and AMBUR (Jackson, 2010; Jackson et al., 2011) provide flexible statistical and geospatial tools within R's ecosystem. Alternative approaches for coastline discretisation include dynamic segmentation (Li et al., 2001), area-based methods (Ali, 2003), and non-linear Gaussian-distribution-based estimation for coastline change measurement (Heo et al., 2009; Kupilik et al., 2017). TBM-based methodologies have become a standard for shoreline behaviour analysis (Sam and Gurugnanam, 2022; Albuquerque et al., 2013) in temperate coastal environments (Mishra et al., 2020), riverbank morphodynamics (Nguyen et al., 2010), bluff crest recession (Brooks and Spencer, 2010), and Arctic coastal erosion monitoring (Jones et al., 2008). In many applications, particularly those involving bluffs and cliffed coasts, linear models have been used under the assumption of a constant erosion rate over time typically fitted using least squares regression (Danforth and Thieler, 1992; Srivastava, 2005) or extended Kalman filters (Himmelstoss et al., 2024). However, this assumption rarely holds in dynamic polar environments, where episodic, abrupt, or non-linear changes are increasingly observed. As coastal erosion patterns become increasingly non-linear, influenced by thermal processes, permafrost dynamics, and marine forcing, modelling approaches must be updated to accurately characterise these changes (Pang et al., 2023; Tsai, 2024).

In Arctic settings, where warming rates are up to four times higher than the global average, SCA has been extensively applied to monitor permafrost bluff erosion, yielding valuable insights into coastal change dynamics (Gibbs et al., 2017, 2019, 2021; Jones et al., 2020; Philipp et al., 2022; Rantanen et al., 2022; Petropoulos et al., 2024). These studies typically employ transect-based approaches or process-based numerical models (Ravens et al., 2012; Barnhart et al., 2014a; Islam and Lubbad, 2022), and are often supported by geospatial datasets or coastal geodatabases (Lantuit et al., 2012; Barnhart et al., 2014a). In contrast, Antarctic applications of SCA remain limited (Sziło and Bialik, 2018; Hrbáček et al., 2023), despite evidence of permafrost degradation in parts of the Antarctic Peninsula and South Shetland Islands (Roland et al., 2024). Given the similarities in environmental forcing mechanisms, insights from the Arctic can be cautiously extended to Antarctic settings, highlighting the relevance of cryospheric processes in shaping coastal retreat and its societal implications (Bronen and Chapin, 2013; Fritz et al., 2017).

Nonetheless, key limitations persist. In polar regions, the scarcity and quality of historical imagery complicate the construction of long-term required imagery datasets (Tsiakos and Chalkias, 2023). Available aerial photographs are often oblique, poorly georeferenced, or collected from heterogeneous sensors (Girod et al., 2018). Identifying shorelines in such data requires manual interpretation, introducing considerable uncertainty (Belova et al., 2022; Ziaja et al., 2023). This uncertainty arises from multiple factors: image scale, observation periods, shoreline proxy definitions, and the spatial-temporal extent of the analysis (Irrgang et al., 2018). Variability in these parameters challenges direct comparisons and model consistency, necessitating robust approaches that explicitly incorporate uncertainty into the analysis (Burningham and Fernandez-Nunez, 2020). To overcome this issue, the statistical models used in analytical tools must explicitly consider uncertainty from various sources, rather than simply weighting data based on image scale. (Himmelstoss et al., 2024; Gómez-Pazo et al., 2022; Jackson et al., 2011).

https://doi.org/10.5194/egusphere-2025-3269
Preprint. Discussion started: 29 September 2025

The current study addresses these challenges by implementing a spatial-temporal analysis based on Shoreline Change Analysis with Transect Based Method (SCA-TBM), applied to a representative coastal bluff system in Port Foster Bay, Deception Island (South Shetland Islands, Antarctica). The site, located between the Argentine Antarctic Base Decepción (BAD) and the Spanish Antarctic Base Gabriel de Castilla (BAEGC), is exposed to rising air and sea temperatures and a shortening sea ice season—factors that contribute to the degradation of volcanic permafrost. Recent erosion assessments using DSAS indicate a clear spatial dichotomy: the south-facing coast is undergoing sustained retreat, while the east-west-facing sections exhibit accretion that poses sedimentation risks to adjacent infrastructure (Torrecillas et al., 2024). Field observations, including those documented in base operations records (Ejército de Tierra: https://ejercito.defensa.gob.es/unidades/Antartica/antartica/, last access: 10 march 2025), suggest that recorded erosion rates may underestimate actual retreat, as evidenced by the recent construction of protective infrastructure at BAEGC.

By analysing a 1.5 km section of bluff ridge as a proxy for coastal change, this research seeks to: (1) quantify local-scale fluctuations in retreat rates, (2) assess the limitations of linear assumptions in dynamic environments, and (3) explore the viability of non-linear modelling strategies to better represent threshold responses and episodic events in bluff evolution. To this end, photogrammetric reconstructions based on archival aerial photography and recent satellite imagery spanning 1956–2023 were used to generate a multitemporal dataset of shoreline positions. Rather than assuming a constant rate of change, the modelling framework evaluates non-linear behaviours and compares traditional linear regression with sigmoidal models, accounting for temporal acceleration and the emergence of retreat thresholds.

This approach not only addresses the methodological constraints of conventional SCA in polar settings but also contributes to a broader understanding of how permafrost-affected coastlines respond to climatic and anthropogenic pressures. The remainder of the paper details the materials and methods employed, followed by the results and discussion of the spatio-temporal patterns observed along the bluff crest. The implications for coastal resilience and monitoring strategies in polar periglacial environments are then considered.

2 Case study location

This study was conducted on a coastal bluff section located within the inner shoreline of Deception Island, part of the South Shetland Archipelago, situated along the northern margin of Bransfield Strait in the Antarctic Peninsula region. Deception Island lies approximately 25 km south of Livingston Island, between 62°53′30″ S and 63°01′20″ S latitude, and 60°29′20″ W and 60°45′10″ W longitude (Figure 1A). The island, a horseshoe-shaped active composite volcano, features a partially submerged structure with an outer diameter of 14 km (N–S) and 13 km (E–W), extending to 25 km at depth (Martí et al., 2013). Access to the inner bay, Port Foster, is via Neptune's Bellows, a narrow southern passage.

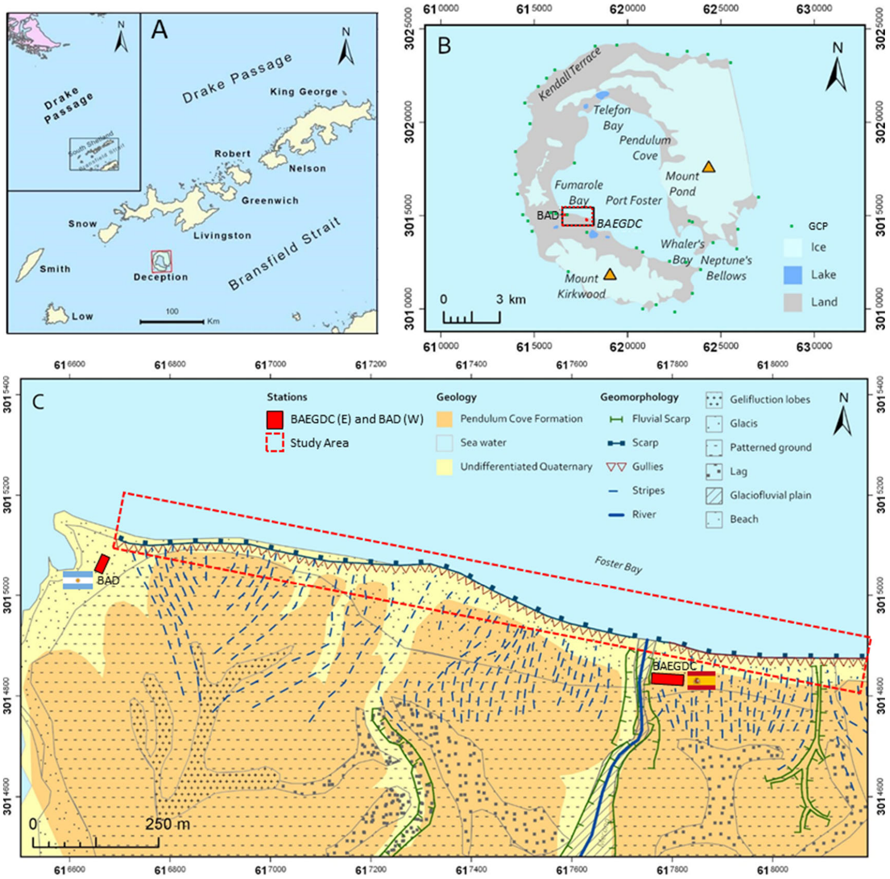

Figure 1. A) Location of study area at Deception Island (South Shetlands, Antarctica Maritime). B) Toponyms, scientific stations and main ice, water and land extents distribution. C) Detailed geomorphology of the cliffed coastal area between Argentinean (BAD) and Spanish (BAEGDC) scientific Antarctic stations in this study (modified from Geological Map of Deception Island in Smellie, 2002, Geomorphological Map of Deception Island in Goyanes, 2015, and de Pablo et al., 2017). Coordinate system UTM WGS84, zone 20S, EPSG:32720.

The island's geomorphology has been shaped by intense volcanic activity, most notably a caldera collapse approximately 3980 years ago, following a VEI-6 eruption (Antoniades et al., 2018). Volcanic activity persisted over subsequent centuries, with notable eruptions in 1842, 1912, 1917, 1967, 1969, and 1970, altering the morphology of both the inner and outer coastlines (Prates et al., 2023). The resulting terrain includes steep caldera walls, glacier-capped peaks such as Mount Pond (539 m) and Mount Kirkwood (452 m) (Figure 1B), and a diverse array of volcanic landforms, including tephra-covered slopes, pyroclastic

https://doi.org/10.5194/egusphere-2025-3269
Preprint. Discussion started: 29 September 2025

deposits, and coastal escarpments. The study area, located between the BAD and BAEGC Antarctic Bases, is notable for its abrupt geomorphic transitions and highly variable cliff morphology (Figure 1C).

The climate of Deception Island is classified as cold maritime polar (Cfc) or tundra (ET) (Peel et al., 2007) under the Köppen (1918) system, but is locally affected by volcanically induced geothermal flux, particularly within the caldera's interior zones (King and Turner, 1997; Caselli et al., 2002; Prieto-Ballesteros et al., 2012). Permafrost is widespread, though patchily distributed where geothermal heating and marine-air interactions elevate ground temperatures. These anomalies contribute to the formation of cryopegs, localised areas of saline, unfrozen ground (de Pablo et al., 2017, 2020).

Since the mid-20th century, the region has experienced accelerated warming. Between 1951 and 2011, the western Antarctic Peninsula recorded a mean temperature increase of 0.54°C per decade (Turner et al., 2014). Recent data (2005–2021) show annual averages of –1.1°C, with maximum and minimum extremes of 12.7°C and –22.5°C, respectively. In contrast, temperatures in the mid-20th century (1948–1967) averaged –2.9°C. Future climate models project a southward shift of the near-surface zero isotherm at approximately 23.9 km per decade (González-Herrero et al., 2024), which, in combination with higher rainfall and decreasing snow persistence, is expected to destabilise the permafrost and intensify coastal erosion.

Marine processes also play a significant role in shaping the island's coastal morphology. The inner bay includes beaches, minor bays, inlets (e.g., Pendulum Cove, Stancomb Cove, Telefon Bay, Fumarole Bay, Whalers Bay), and seasonal river mouths, shaped by rocky headlands (Figure 1b). Tidal dynamics are complex, with a mixed semi-diurnal regime influenced by primary tidal constituents M2, S2, O1, and K1. Seasonal tidal ranges vary between 0.8 m and 2.7 m, with meteorological tides adding up to 0.7 m during storm events (Vidal et al., 2012; Antelo et al., 2015; Figueiredo et al., 2018). Wave energy within Port Foster is modulated by a 6.5 km fetch, producing significant wave heights up to 1.165 m, with observed breaker-zone heights of 0.97 m and run-up levels of 0.5 m (Caballero, 2023). These hydrodynamic forces contribute to the weathering and mechanical undercutting notch of cliff bases, particularly in unconsolidated sections. The outer coastline, in contrast, is dominated by the Outer Coast Tuff Formation, with steep volcanic cliffs several tens of metres thick, incised by glacial action and exposed to open sea conditions (Martí et al., 2013; Hopfenblatt et al., 2022). Small pocket beaches have formed at the base of these cliffs, often inaccessible except by boat, highlighting the erosional complexity of the island's exterior margins shaped by regional marine dynamics.

The selected 1.5 km bluff segment between BAD and BAEGC exhibits a substrate that includes both lithified and non-lithified pyroclastic materials, unconsolidated heterometric tephra, such as ash, lapilli, and scattered larger pyroclasts, making the terrain especially prone to rain-induced surface runoff and wave attack (Figure 1c). The study site is lithologically characterised by the Pendulum Cove Formation, composed of post-caldera pyroclastic flows and ashfall deposits, with nearshore surfaces overlaid by the undifferentiated Quaternary formation, formed through remobilisation by solifluction and fluvial processes (Smellie, 2002). Lithologically, the material consists of poorly graded silty sands with variable grain sizes, from fine ash to bomb-sized lapilli fragments (ASTM, 2000). The vertical stratigraphy is organised into three geotechnical units (GUs): (i) the active layer (GU-AL) is 0.3–0.9 m thick in summer, with an average temperature of –0.5°C (de Pablo et al., 2015, 2017); (ii) beneath it, the permafrost unit (GU-PF) extends from 2.5 to 9 m, remaining perennially cryotic (Vieira et al., 2008; Ramos et al., 2017); (iii) the subpermafrost unit (GU-ST) contains saturated or unfrozen material, often underlain by cryopeg zones, where salinity prevents freezing (González-Posadas et al., 2022).

While BAD is located on a beach, BAEGC sits on a raised on the plateau back side of the coastal bluff ridge with a fronting beach, transitioning eastward into a more pronounced cliff ridge (Paredes et al., 2021). The northern orientation of most of the bluff increases exposure to solar radiation, while the eastern sector (N88E) lies downwind of prevailing south-westerly winds, enhancing aeolian and moisture flux. The cliff base shows signs of active erosion through thermoerosional niches and shallow gullies, attributed to ephemeral summer meltwater runoff and suffusion-driven sediment transport, forming transient dejection cones that are rapidly reworked by wave action (López-Martínez et al., 2012; González-Posadas, 2019).

Surface temperatures fluctuate seasonally from 5°C in summer to –5°C in winter, with more intense variability near anthropogenically altered zones. The mean annual temperature of the upper 0.6 m remains near –0.5°C, rendering the underlying permafrost particularly sensitive to climatic and mechanical disturbance (Streletskiy, 2021). During winter, frozen surfaces impede water flow, while in summer, snowmelt, rainfall, and anthropogenic heat flux promote active-layer deepening, slope instability, mudflows, and gully formation—all of which compound coastal recession. These processes reflect a dynamic feedback between atmospheric warming, surface hydrology, and marine energy, which together contribute to the destabilisation of the cliff face.

3 Multitemporal imaging geoinformation

Various cartographic representations of the island have been created at different scales using different geodetic systems and projections (Prates et al., 2023). This has made it difficult to accurately assess temporal changes in the island's terrestrial features. Characterising potential changes in coastal dynamics requires a multi-temporal database. Sets of images from historical flights, satellite optical images and current SAR images have been used to extract the catalogue of the historical, recent and present inner coastline south-west of Port Foster. Each set is pre-processed for georeferencing, orthorectification and mosaicking.

3.1 Archive aerial imagery

Adverse meteorological conditions and operational constraints have historically limited aerial photographic missions over Deception Island. Only four historic aerial flights—conducted in 1956, 1968, 1979, and 1986—are available, and all have been incorporated into this work (Table 1).

The earliest dataset was produced by the Falkland Islands Dependencies Aerial Survey Expedition (FIDASE) in December 1956. This mission aimed to systematically photograph the island vertically (Mott, 1986), using a Williamson Eagle IX camera with a 152 mm focal length and a Ross 6" lens. The imagery was captured at altitudes of 3962 m and 4390 m with scales of 1:26000 (dec/17th/1956) and 1:28800 (dec/19th/1956) respectively (Brecher, 1975). Exposure times ranged from 1/200 to 1/50 seconds, and image sets consisted of two overlapping (60% longitudinal and 30% a lateral overlaps) series with 31 and 22 photographs. Eight astronomically triangulated control points and the proximity of nearby South Shetland Islands provided geodetic support for the mission. Scanned at 1016 dpi (10002 × 10002 pixels), the dataset has facilitated stereo-photogrammetric restitution of otherwise inaccessible regions of the Antarctic Peninsula (USGS EarthExplorer: https://earthexplorer.usgs.gov/, last accesed: 1 June 2025).

Table 1. Characteristics of archival aerial image acquisition from historic flights.

Flight survey data	FIDASE 1956		SHNA 1968	BAS 1979	SAF 1986
Flying altitude	4390 m	3962 m	4 650 m	1828.8 m	2400 m
Scale	1:28800	1:26000	1:30000	1:16000	1:30000
Camera model	Williamson Eagle IX		K-17 6”	MK2 n.1171	Zeiss RMK 23/8
Focal length	152 mm		152.4 mm	152.87 mm	85.59 mm
Scan resolution	9761x9868		5400x5400	15634x15109	13080x13735
No. photo scanned	31	22	33	221	22
No. of flight tracks	3		4	2	2

A second flight, undertaken by the Argentine Navy on 21 January 1968, followed significant volcanic activity in December 1967. The mission, executed by the Argentine Hydrographic Service (SHNA), employed a K17 camera with a 152.4 mm focal length. Conducted at 4500 m with a 1:30000 scale, the mission acquired 33 images across four passes (60% longitudinal and 20% a lateral overlaps). Despite its historical value, the scanned non-photogrammetric resolution (5400 × 5400 pixels at 96 DPI) and absence of precise calibration parameters posed additional processing challenges.

The third mission, led by the British Antarctic Survey (BAS) on 7 March 1979, markedly differed from the others by operating at a much lower altitude of 1828.8 m. A total of 221 images were acquired (124, RN 139/1737 RN 4/79 and 97, 1360/1737 RN5/79) from a Royal Navy helicopter using an F49 MK2 camera with a 152.87 mm focal length. High-resolution scanning (15634 × 15109 pixels at 1600 dpi) enabled accurate surface reconstructions. This set offered the finest detail among the historical flight and was key to resolving morphodynamic nuances at bluff scale.

The last historical imagery set stems from a 1986 campaign by the Chilean Air Force's Aerial Photogrammetric Service (SAF), using a Zeiss RMK 23/8 camera (85.59 mm focal length). Comprising two passes (eight images on 14 January and fourteen on 21 December), this mission covered the island’s eastern and western sectors at a 1:30000 scale, and the used digital images have a horizontal and vertical resolution of 1400 dpi. However, disparities in acquisition dates and limited ground control in the eastern sector affected georeferencing accuracy.

3.2 Satellite imagery

To bridge the 15-year gap between the 1986 aerial mission and the emergence of high-resolution satellite imagery, eight optical satellite images (2001–2013) were integrated into the dataset (Table 2). Images from the IKONOS-2, QuickBird-2, GeoEye-1, and WorldView-2 platforms were acquired with cloud cover below 40%. The QuickBird-2 image from 2005 was selected as the ground base for georeferencing all other satellite scenes due to its optimal clarity and coverage.

Table 2. Parameters of satellite images from the recent past: Date: date of acquisition, SS: satellite sensor, CC: cloud cover in the full image, GSD: maximum ground sampling distance, ION: image tilt, SE: sun elevation / orbit. *Image © 2025 Maxar Technologies, **Image U.S. Geological Survey.

Catalogue (dd/mm/yyyy)	Satellite platform*	CC (%)	GSD (m)	ION (°)	SE (°)
07/12/2001	IKONOS 2**	47.0	0.86	10.8	43.3
15/01/2002	IKONOS 2**	9.0	0.80	22.5	42.1
11/03/2003	IKONOS 2	3.0	0.99	27.1	26.0
21/01/2005	QuickBird 2	0.0	0.68	14.4	34.4
03/01/2010	IKONOS 2	16.0	1.11	31.5	44.5
16/10/2010	GeoEye 1	26.0	0.46	17.7	30.6
04/12/2013	WorldView 2	0.0	0.58	25.7	43.1
29/12/2013	WorldView 2	0.0	0.57	24.9	41.9
2019	PAZ	SAR	0.6	Ascending	
2020	PAZ	SAR	0.6	Ascending	
2021	PAZ	SAR	0.6	Ascending	
2022	PAZ	SAR	0.6	Ascending	

To supplement optical datasets, four synthetic-aperture radar (SAR) images were incorporated from the PAZ mission (2019–2022). Acquired in ascending orbital passes, these X-band SAR images offered a resolution of 0.6 m per pixel. Each image was orthorectified against the 2005 Digital Terrain Model (DTM) provided by the Army Geographic Centre using the Sentinel SNAP toolbox (ESA, 2024), which includes terrain deformation correction features. SAR image geolocation errors were derived directly from PAZ documentation (Bonilla et al., 2024).

https://doi.org/10.5194/egusphere-2025-3269
Preprint. Discussion started: 29 September 2025

Following pre-processing, all raster layers were harmonised spatially within a GIS framework. This multitemporal geospatial foundation formed the basis for delineating shoreline reference lines (Ankrah et al., 2022), which are analysed further using the TBM-based Shoreline Change Analysis methods described in subsequent sections.

4 Methods

This study employed a quantitative approach to SCA based on the Transect-Based Methodology (TBM) for evaluating cliff-top retreat. The objective was to determine and model the net spatial displacement of the bluff crest through temporal analysis of georeferenced imagery. This approach enabled the calibration of both linear and non-linear regression models of erosion behaviour across defined sections of the study area. Historical aerial photographs (Table 1) and more recent satellite imagery (Table 2), both optical and SAR-based, were orthorectified and spatially aligned using a unified ground control framework based on the QuickBird2 image dated 21 January 2005.

A GIS-based workflow was implemented to digitise the cliff-top as a reference line (Himmelstoss et al., 2006) and its associated positional uncertainty for each orthorectified image. This dataset spans a 66-year time series from 1956 to 2022. The resulting reference lines were discretised via a transect system anchored to a fixed baseline, allowing calculation of shoreline change metrics, uncertainty-weighted rates of change, and derivation of morphodynamic insights from fitted regression models.

4.1 Photogrammetric pre-processing and image georeferencing

A photogrammetric restitution process was undertaken to construct orthoimage mosaics from scanned images of the four archival aerial flights (Table 1). The increased computational efficiency and capabilities of Structure-from-Motion (SfM) and Multi-View Stereo (MvS) techniques have revolutionised photogrammetric processing, offering viable alternatives to traditional stereo restitution (Cook, 2017). This method facilitates the reconstruction of dense point clouds by identifying homologous features across multiple overlapping images and calculating their spatial coordinates relative to the camera reference frame.

The full 3D reconstruction pipeline requires knowledge of ground control points (GCPs) and camera centre (CC) positions within a consistent reference system. Outputs include a dense point cloud (DPC), a triangulated irregular network (TIN), a digital elevation model (DEM), and a high-resolution orthorectified mosaic image (HROM). However, the application of SfM-MvS to historical aerial imagery in polar environments presents numerous technical challenges (i.e. Riquelme et al., 2019). These include missing camera calibration data (e.g. FIDASE 1956), eroded or absence of fiducial marks (e.g. SHNA 1968, BAS 1979, SAF 1986), high flight altitudes, large image scales, and scanning artefacts or surface damage.

Despite these limitations, a refined SfM-MvS workflow was implemented using Agisoft Metashape PhotoScan Professional (v2.1.3, Agisoft LLC, St. Petersburg, Russia), based on the protocols proposed by Over et al. (2021) to overcome the differences and quality criteria to get the DPCs, TINs and HROMs (Child et al., 2021; Prates and Vieira, 2023; North and

Barrows, 2024, among others). The optimisation focused on minimising three main sources of error in the outputs: Uncertainty Reconstruction (UR), Projection Precision (PP), and Reprojection Error (RE). Acceptable thresholds were set as follows: UR ≤ 10, PP ≤ 10, RE ≤ 1 pixel, contingent on image quality (Paredes et al., 2021). A total of 37 stable GCPs were selected for this process. These were identified both in the historical images and in the QuickBird2 image, primarily consisting of immobile rocky outcrops and promontories unaffected by volcanic or cryospheric changes since 1956 (Figure 1b). GCPs were georeferenced using WGS84 - UTM20S (EPSG:32720), providing positional consistency across image sets and contributing to the elevation restitution of each orthophoto mosaic. Each historical flight was processed individually, generating TIN, DTM, and HROM outputs for subsequent analysis.

For satellite optical images downloaded from Google Earth Pro (Google: https://www.google.es/intl/es/earth/versions/, last accessed: 1 June 2025) georeferencing was required due to the absence of embedded spatial metadata. Each satellite image was manually rectified against the QuickBird 2 (01/21/2005) reference image using a map-to-map georeferencing strategy in a GIS environment. GCPs were selected from persistent landscape features and built infrastructure (e.g. buildings at BAD and BAEGC), ensuring uniform spatial distribution and optimising georeferencing accuracy. Due to varying image characteristics (illumination, contrast, resolution), not all GCPs were detectable across all satellite scenes. A minimum of ten GCPs per image was employed, and spatial accuracy was quantified using root mean square error (RMSE) metrics.

In contrast, SAR images from the PAZ mission do not require georeferencing, as they are provided with intrinsic geolocation metadata. Nonetheless, orthorectification is essential to correct geometric distortions introduced by sensor tilt and terrain variability. Without such corrections, image displacement can compromise the spatial accuracy of morphometric analyses, particularly in topographically diverse coastal environments. To correct SAR imagery, the Range Doppler Terrain Correction (RDTC) algorithm (Small and Schubert, 2019) was applied using the SNAP toolbox (ESA, 2024), with elevation data from the REMA DEM (Howat et al., 2019). This ensured geocoded rectification of all SAR images from 2019 to 2022, yielding terrain-adjusted products suitable for integration into the time series.

4.2 Extraction of Reference Lines and Uncertainties

A valid shoreline change analysis (SCA) requires a reference line that can be clearly identified in each of the multitemporal images used (Boak and Turner, 2005). For this study, the reference line was manually interpreted from each image in a GIS environment and positioned along the bluff crest, where visual evidence of geomorphic change was most reliably captured. The visibility of this crest is typically more consistent across the diverse image catalogue than that of the cliff base, which is often obscured by shadow or backshore debris. The decision to trace the crest or erosion scarps, rather than the foot (Figure 2), of the coastal bluff was influenced by the limitations of available data: DEMs derived from historical flights lack the necessary resolution, and no full temporal DEM sequence exists to support automatic tracing of slope breaks (Young et al., 2009; Farquharson et al., 2018). Figure 2 presents the conceptual model used for reference line delineation. On this model, the reference line (yellow) is traced along the visible ridge of the bluff on a consistent digitising plane. The associated uncertainty band (between the red and green lines) accounts for visual ambiguity and potential digitisation error. The red line represents the perceived start of the bluff's face when viewed from above, while the green line marks the transition into the inland plain or attenuated slopes. Furthermore, the visual conditions—affected by sun angle, shadow length, and surface contrast—often render the base of the bluff indistinct, while the crest maintains relatively stronger visual continuity across all imagery.

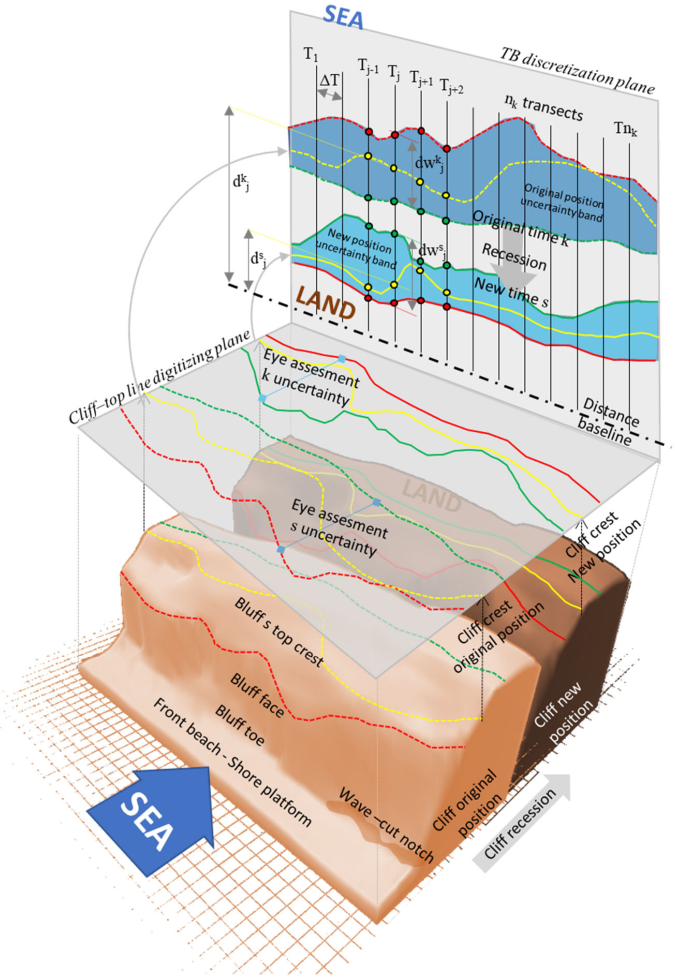

Figure 2. Block diagram of the coastal bluff on which the reference lines and their uncertainty bands are delineated (in the digitising plane), and the TBM is applied for their discretisation (in the discretisation plane).

The wide heterogeneity of image types and qualities (Tables 1 and 2) ruled out the use of automated edge detection or segmentation techniques across the full dataset. Semi-automatic tracing, although promising in controlled conditions (Tsiakos and Chalkias, 2023; Philipp et al., 2022; Kazhukalo et al., 2023; Tsai, 2024; Scala et al., 2024; Lu et al., 2024), was impractical due to the inconsistent resolution, contrast, and illumination across the 66-year imagery archive. Instead, the reference line was manually traced by a single operator to ensure consistency. To aid this visual interpretation, histogram equalisation (HE) technique were applied to each image, improving contrast in colour channels and facilitating the identification of geomorphic markers relevant to the crest of the bluff. HE is an effective and well-established method of indirect contrast enhancement, whereby the image histogram is modified (see, for example, Vukadinov et al., 2017). The combination of histogram equalisation across different colour ranges serves to highlight certain morphological changes and other coastal features, including the band in which it is visually located (the s^{th} ridge of the bluff) and the manual tracing of the sought ridge (Figure 2, yellow line) on a common digitising plane.

Errors in the precise placement of reference lines stem from several factors: (1) resolution limitations of older imagery; (2) diffuse morphological expression of the bluff crest; (3) variable viewing altitudes and angles; and (4) reduced contrast in snow-covered or shadowed areas (Warnasuriya et al., 2020). These sources of error were addressed by plotting an uncertainty band around each digitised crest line. This band, manually delineated (Figure 2, band between the red and green lines), reflects the operator's judgement of the plausible spatial range within which the crest might reasonably lie based on visual and morphological cues. This procedure was repeated for each image date, producing a time-series catalogue of crest reference lines (e.g. k^{th} bluff crest) and associated uncertainty bands (e.g. k^{th} uncertainty band). These features were projected in zone 20S (EPSG::32720) and stored as polygons within a GIS-based geodatabase for further analysis.

To quantify the uncertainty associated with each line, the width of the band between the red and green boundaries was measured for every digitised transect. These distances were calculated for the n^k j-points where the reference lines were discretised (yellow dots in Figure 2) using the TBM and uncertainty band boundaries (red and green dots in Figure 2). This uncertainty width, denoted as dw_j^k, was later used in the statistical treatment of the distance-time datasets. The spatial variation in band width across transects and time was assessed to inform weighting strategies in subsequent shoreline change modelling.

The cumulative effect of these uncertainties—arising from kth-image resolution (GSD^k), photogrammetric orthorectification (GE^{k1}), georeferencing errors (GE^{k2}), and manual digitisation (d_j^k)—was integrated into a total uncertainty metric Et_j^k, calculated using the following root sum square formulation (Hapke et al., 2006; Ruggiero et al., 2013):

$$\mathrm{Et}_j^k = ((\mathrm{GSD}^k)^2 + (\mathrm{GE}^{k1})^2 + (\mathrm{GE}^{k2})^2 (\mathrm{dw}_j^k)^2)^{1/2} \tag{1}$$

This error metric was computed for each time step k (k ≡year: 1956, 1968, 1979, 1986, 2001, 2002, 2003, 2010.01, 2010.10, 2013, 2019, 2020, 2021, 2022), and transect j = 1,… NT total number of outlined transects. Each Et_j^k value is incorporated in the least square models within SCA by means of a weighting scheme (Table 3). Then, the normalized weight W_j^k is calculated according to the following formula:

$$\mathrm{W}_j^k = \mathrm{w}_j^k / \textstyle\sum_{i=1}^{NT} \mathrm{w}_j^k \tag{2}$$

Table 3. Expressions of the weights used in this work to incorporate the multiple sources of uncertainty in the data.

Weights (k: year index, j: transect index)	Inverse square (ISQ)	Exponential (EXP)
Non-standarized (**NS**)	$w_j^k = 1/(Et_j^k)^2$	$w_j^k = e^{0.3Et_j^k}$
Standarized (**ST**) $\mu E^k = (\sum_{j=1}^{n^k} Et_j^k)/n^k$ $\sigma E^k = \left[(\sum_{j=1}^{n^k} Et_j^k - \mu E^k)/n^k\right]^{1/2}$ $\omega Et_j^k = Et_j^k \, \sigma E^k / \mu E^k$	$w_j^k = 1/(\omega Et_j^k)^2$	$w_j^k = e^{0.3\omega Et_j^k}$

All extracted and weighted reference lines and uncertainties were prepared for transformation into the TBM discretisation system (Figure 2), the subject of the following subsection.

4.3 Shoreline change statistics

The SCA was performed using Shoreline Change Statistics (SCS), assessing both linear and non-linear trends over time (Dolan et al., 1991; Fenster et al., 1993). Reference lines and their uncertainty bands were transformed into a point cloud through the Transect-Based Method (TBM), intersecting with a series of equidistant transects (T_j) spaced at 5 m intervals (Figure 2), allowing for consistent discretisation across the coastal stretch (Warnasuriya, 2023).

The distances d_j^k from each shoreline reference line to a fixed inland baseline were calculated for all time points and transects. These values were weighted by W_j^k based on the total uncertainty Et_j^k within the least square regression framework of SCS. All statistical computations were implemented in the MATLAB-based CREES software tool (Cliff Recession Enhanced Estimation and Simulation). For each transect and time sequence, CREES computes: (i) Shoreline Change Envelope (SCE): the maximum range between recorded shorelines; (ii) Net Shoreline Movement (NSM): distance between earliest and latest shoreline positions; (iii) End Point Rate (EPR): shoreline movement over elapsed time. CREES also calculates weighted descriptive statistics, including covariance and Pearson's correlation, to evaluate the dependence between shoreline position and time, assessing the extent of linearity across each T_j transect.

4.4 Regression least square models

Each distance-time pairs (d_j^k, t^k) time-series (t^k in days since an arbitrary time origin) per j^{th}-transect was fitted using ordinary least squares (OLS) regression. To reduce the influence of outliers, robust regression was applied through reweighted least squares RWLS (Genz et al., 2007), using a minimisation criterion for weighted residuals (Rousseeuw and Leroy, 2003). Once an arbitrary model D(t) is selected accordingly to the (d_j^k, t^k) time-series observed behaviour, the residual sum of squares or sum of squares error (SSE_j) was minimised, for each j=1…NT, as follows:

$$SSE_j = \sum_k W_j^k (d_j^k - D(t^k))^2 \tag{3}$$

Here, model D(t) fitting included both standard linear in SCA software (Danforth and Thieler, 1992; Jackson et al., 2011; Gómez-Pazo et al., 2022, among others) and non-linear forms (Table 4). Thus, in addition to the standard linear model, second-order polynomial, logistic sigmoid, and Gompertz models were used to describe varying recession dynamics, including potential acceleration phases (Fenster et al., 2001; Tsai, 2024). Instantaneous recession rates, R(t)=dD(t)/dt, were derived from each fitted model to track temporal changes.

Model performance was evaluated in CREES, for each fitted model (Table 4) minimizing Eq. (3), using: (i) R^2: goodness of fit, (ii) STDE: standard error of estimate, (iii) AICc: corrected Akaike information criterion, (iv) 95% CI: confidence interval of the rate. Transect dynamics were classified into (Tsai, 2024): (i) Random: if $R^2 < 0.6$ for all models, (ii) Correlated: if one model exhibited highest R^2 and lowest AICc and STDE. This classification supports the identification of spatial trends in coastal behaviour and enables robust interpretation of bluff recession patterns.

Table 4. Different models used in this work for of discrete distance-time D(t) vs. t data least squares regression, and its instantaneous derived velocity R(t).

Model name {parameters}		Model equation D(t)	Instantaneous recession rate R(t) = D'(t)
Linear {a,b}	LM	$a + bt$	b
Quadratic {a,b,c}	QM	$a + bt + ct^2$	$b + 2ct$
Sigmoidal Logistic 3p {a,b,c}	SL3	$\frac{a}{1 + e^{-b(t-c)}}$	$\frac{abe^{-b(t-c)}}{(e^{-b(t-c)} + 1)^2}$
Sigmoidal Logistic 4p {a,b,c,d}	SL4	$d + \frac{a - d}{1 + (t / c)^b))}$	$\frac{b(a - d)(t / c)^b}{t((t / c)^b + 1)^2}$
Sigmoidal Gompertz {a,b,c,d}	SG4	$d + (a - d)e^{-e^{b(c-t)}}$	$b(a - d)e^{b(c-t)-e^{b(c-t)}}$

5 Results

5.1 Photogrammetric pre-processing and image georeferencing

All historical aerial images were processed in Agisoft Metashape to generate orthorectified mosaics, enabling their integration into a unified geospatial framework (WGS84 - UTM20S, EPSG::32720). Ground Control Points (GCPs) were visually identified across stable features—such as rocky promontories and infrastructure at BAD and BAGC—and used to correct each flight set. Over 30 GCPs were employed per flight, ensuring sub-metre Ground Sampling Distance (GSD). The resulting Root Mean Square Errors (RMSE) for these historical orthoimages ranged from 0.76 m to 22.7 m, depending on image quality, flight characteristics, and the number and distribution of GCPs (Table 5). Typically, over 30 GCPs were used per flight. However, for the SAF 1986 series, which consisted of two acquisition passes taken on different dates, the georeferencing relied on only 16 GCPs for the western half, resulting in higher RMSE values, particularly in the western half.

Satellite images (2001–2013), although ortho-projected, lacked spatial referencing and were therefore georeferenced using the 2005 QuickBird2 image as a reference. Between 15 and 21 GCPs were placed on persistent geomorphic features—mainly rocky outcrops and structural landmarks at the research stations—to conduct geometric correction via second-order polynomial transformation. Resulting RMSEs ranged from 0.3 to 2.5 m, with all images maintaining GSD values below 1 m, ensuring suitable spatial resolution for cliff-top identification.

The photogrammetric processing of all imagery—historic aerial and optical satellite—was performed within a coherent spatial framework. This alignment facilitated consistent shoreline reference line digitisation and uncertainty band delineation across the 66-year image sequence. The resulting high-resolution, georeferenced datasets form the analytical basis for the subsequent shoreline change analysis and regression modelling.

Table 5. Quality indexes of multitemporal spatial imaging geoinformation after processing: orthophotogrammetric restitution for archival images, georeferencing for optical satellital images and RDTC correction for PAZ images.

Imaging source		No. GCP	GSD (m)	Pixel Acc. (m)	RMSE (m)
FIDASE 1956	FD56	37	0.77	4.7	3.28
SHNA 1968	SH68	35	0.72	3.6	2.93
BAS 1979	BA79	36	0.18	11.6	6.32
SAF 1986 west	SA86	16	0.44	23.7	22.7
IKONOS2 2001	IK01	15	0.86	0.65	0.76
IKONOS2 2002	IK02	26	0.8	1.69	2.07
IKONOS2 2003	IK03	16	0.99	1.87	2.47
QUICKBIRD 2005	QB05	-	0.68	0.62	0.3
IKONOS2 2010	IK10	16	1.11	1.33	1.69
GEOEYE1 2010	GE10	21	0.46	0.78	0.92
WORLDVIEW2 2013	W213	21	0.58	1.07	1.30
WORLDVIEW1 2013	W113	21	0.57	0.66	0.78
SAR PAZ 2019	SP19	-	0.6	0.1	0.07
SAR PAZ 2020	SP20	-	0.6	0.1	0.07
SAR PAZ 2021	SP21	-	0.6	0.1	0.07
SAR PAZ 2022	SP22	-	0.6	0.1	0.07

5.2 Extraction of reference lines and shoreline change statistical analysis

Following image pre-processing, georeferencing, and correction, reference lines and uncertainty bands were manually delineated in a GIS environment. This was performed by a single trained operator using HE techniques to enhance visual contrast across RGB channels, facilitating consistent interpretation of 16 shoreline positions spanning the period 1956–2022 (Figure 3A). Despite challenges such as snow cover and low contrast in certain image sets, the method enabled reliable delineation of the bluff crest for each date. The furthest inland and nearest coastal positions, derived from contrast differences, were used to define maximum and minimum polygons representing the uncertainty band for each reference line (Figure 3B). The resulting polygonal bands were transformed into point datasets by the TBM, generating discrete points every 5 m across a total of 294 transects oriented approximately east–west. This resolution was deemed adequate for characterising spatially heterogeneous recession patterns while maintaining analytical tractability.

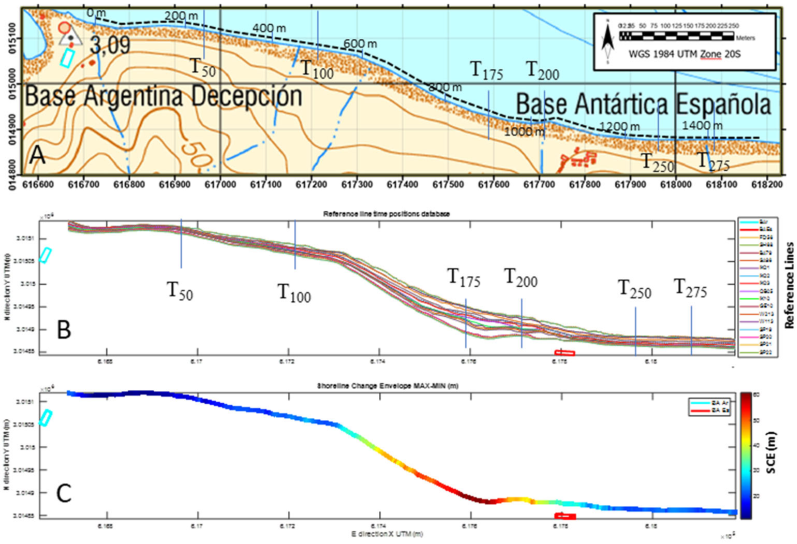

Figure 3. A) Detail in the study area marking the distances over the coastline measured from the western boundary and three of the control transects selected in this work (T50, T175 and T275). B) Catalogue of 16 polygonal lines extracted from the processing of the images in the study area and their discretisation into points with TBM (points on the polylines). C) Shoreline change envelope (SCE) between the first reference line (FIDASE 1956) and the last one (SAR PAZ 2022).

The Shoreline Change Envelope (SCE) captured the largest retreat values—up to 60 m—within the central third of the study area, particularly around the left bank of the Mekong River estuary, the only easterly-facing coastal segment (Figure 3C). These high rates of displacement illustrate the intensified retreat in segments exposed to direct wave energy. Conversely, shoreline sections adjacent to the BAD station showed minimal change, averaging under 11 m, while much of the remaining coastline experienced shifts below 30 m. The segment fronting the BAEGC, with a mostly north-facing orientation, exhibited intermediate retreat values in the 30–40 m range.

Uncertainty analysis revealed a diverse range in the band widths dw_j^k between the maximum and minimum line for each year. Values ranged from 1.2 m to 39 m, the latter seen in low-contrast imagery from GE1 2010. Despite such exceptions, 90% of the uncertainty widths were below 15 m. and interquartile ranges for most transects fell between 5 m and 10 m, with a small number of outliers due to variable image quality. No consistent spatial clustering of uncertainties was observed along the cliff, although a general temporal trend was evident—recent imagery consistently yielded narrower uncertainty bands and lower variance. This reflects improvements in resolution and sensor calibration over time.

Once incorporated these uncertainties, distance-time data points were weighted according to a composite measure in Equation (1), with normalisation applied as per Eq. (2) and equations in Table 3. High-resolution, recent imagery received higher weights (closer to 1), contributing more strongly to regression analyses and statistical estimates. Earlier or lower-quality datasets with larger uncertainty bands were included but down weighted accordingly, minimising distortion in model outcomes.

Using the weighted distance-time dataset, descriptive statistical analysis was conducted across all transects. Sample covariances (Figure 4A) and Pearson's correlation coefficients (Figure 4B) were calculated to assess the linearity and strength of shoreline evolution over time. In all cases, both statistics were negative, confirming a general retreat trend. Pearson's correlations ranged from -0.78 to -1.0, while the weighted correlations ranged between -0.77 and -1.0, indicating improved robustness in the presence of uncertainty. However, covariances exhibited notable oscillations along the transect axis, particularly across the central third of the study area, where values approached -140×10^3. These spatial fluctuations suggest that erosion dynamics are not uniformly distributed and may be influenced by local geomorphological or exposure conditions. Despite incorporating differential weighting, the pattern of statistical dependence between shoreline positions and time remained broadly consistent, confirming the robustness of the SCA-TBM framework and the analytical processing applied.

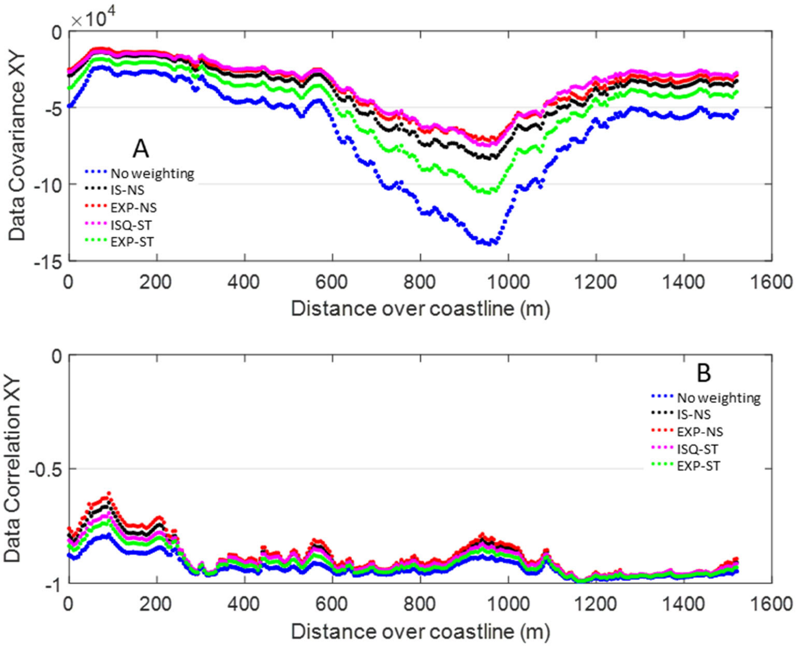

Figure 4. A) Data Covariance and B) Pearson's correlation coefficient related with distance travelled along the coastline from western initial point.

5.3 Regression least square models

The application of the classical Shoreline Change Analysis (SCA) using a linear regression model (LM, Table 4) was conducted over the 294 transects across the study area. The estimated rates of change (Table 1) show consistently negative slopes $R(t) = b < 0$, indicating coastal recession. The regression-adjusted LM revealed significant spatial variability along the coastline. For instance, the distribution of distance versus time data across transects (three of them in Figure 5A) E-W transitions from a moderately decreasing pattern (i.e. at T_{50}) with correlation ≈ -0.75, to a linear trend (i.e. at T_{100}) with correlation ≈ -0.93, and even stronger correlations < -0.98 (i.e. at T_{250}). Despite this high negative correlation, noticeable data dispersion around the regression lines persists. Narrowing of 95% confidence intervals towards more recent observations highlights the increasing reliability of later data due to reduced errors.

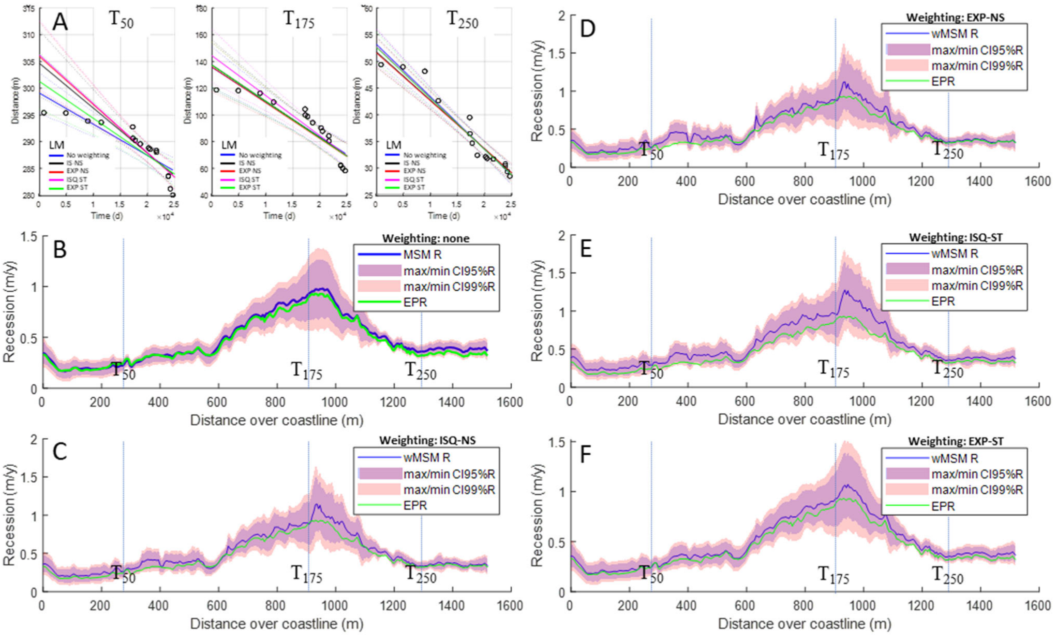

Figure 5. LM regression results: A) detail of the fitted LM to distance vs. time (days since FD56) at transects 50, 175 and 250 (solid lines) and their 95% prediction bounds across the LM fit range (dotted curves around each linear model), applying the four weighting schemes considered in this work (Table 3) and without weighting. Recession R (in m/y) fitted with the ML (blue line) by least squares method (MSM) with the confidence intervals (CI) on R (at 99% and 95%) and the end-point rate (EPR, plotted with green line) at each transect along the study area, in B) recession result (MSM R) without weighting, in C) recession result (wMSM R) with weighting (ISQ-NS), in D) recession result (wMSM R) with weighting (EXP-NS), in E) recession result (wMSM R) with weighting (ISQ-ST), and in F) recession result (wMSM R) with weighting (EXP-ST). In each graph the location of the transects T_{50}, T_{175}, T_{250} used in A are marked.

The LM outputs identify three distinct spatial zones (Figures 5B-F). The western segment (T_1–T_{125}, along shore range 0–600 m) exhibits modest recession rates ($b < 0.5$ m/y), with a mean of 0.25 m/y. These rates closely match the EPR, with narrow 95% and 99% confidence intervals. Residuals are tightly confined within ±2 m, and interquartile ranges rarely exceed 1 m. The central segment (T_{125}–T_{215}, along shore 600–1100 m) shows the highest recession rates (1.0–1.15 m/y), especially near the mouth of the Mekong River. This region also exhibits larger 90% and 95% confidence intervals and the highest residuals, ranging ±4 m, with interquartile spreads of about 3 m. The easternmost segment (T_{215}–T_{294}, along shore range 1100–1500 m) features intermediate recession rates ($b \approx 0.5$ m/y), with smaller uncertainties and interquartile ranges around 0.5 m.

The quadratic model (QM) regression, independent of weighting, produced initial positive rates $R(t)>0$ (up to 1 m/y), notably at T_{50} and T_{175}, before transitioning to negative rates (Figure 6A). These trends highlight a maximum in shoreline position $D(t)$ around 2000, after which consistent recession accelerates until 2023, reaching -3 m/y at T_{175} and -0.45 m/y at T_{250}. These results imply a temporally non-linear accretion/erosion behaviour. Space-time maps of $R(t)=b+2ct$ confirm this zonal structure

(Figures 6B-F). The first zone (T_1–T_{125}) saw $R(t) < 1$ m/y by 2023, with earlier acceleration. Despite low sensitivity to weighting, this zone shows the widest 95% confidence intervals (up to 14 m), which narrow markedly over time. The second zone (T_{125}–T_{210}) is marked by recession rates close to 2.5 m/y by 2023. The third zone (T_{210}–T_{294}) displays persistent $R(t)<0.5$ m/y, with minimal temporal variation.

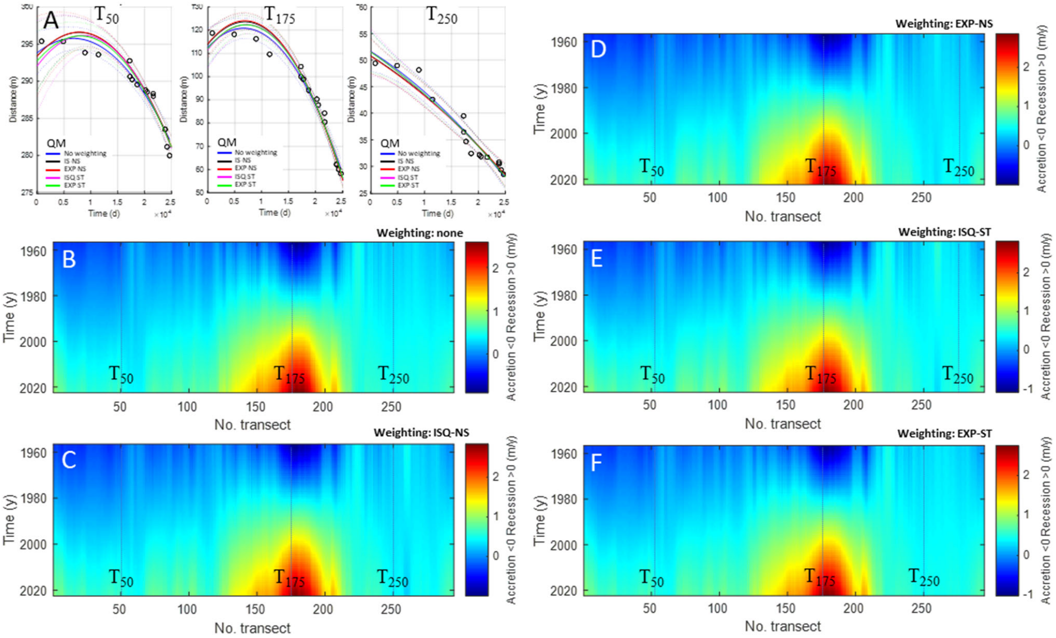

Figure 6. QM regression results: A) detail of the fitted LM to distance vs. time (days since FD56) at transects 50, 175 and 250 (solid parabolas) and their 95% prediction intervals across the QM fit range (dotted curves around each parabolic model), applying the four weighting schemes considered in this work (Table 3) and without weighting. Instantaneous recession R(t) map (in m/y) fitted with the QM (R(t) in Table 4) along the time interval [1956, 2022] for each j^{th} transect (j=1..294) along the study area, in B) R(t) map without weighting, in C) R(t) map with weighting (ISQ-NS), in D) R(t) map with weighting (EXP-NS), in E) R(t) map with weighting (ISQ-ST), and in F) R(t) map with weighting (EXP-ST). In each graph the location of the transects T_{50}, T_{175}, T_{250} used in A are marked.

Sigmoidal regression models—SL3, SL4, and SG4— (Figure 7) are more sensitive to weighting, as seen at T_{250} and T_{275} (Figure 7H, 7I). Here, in unweighted fits, they failed to capture acceleration phases accurately, while weighted fits exhibited steeper sigmoid curves. All three sigmoidal models (SL3, SL4, SG4) successfully captured monotonic decreases in shoreline position $R(t) \leq 0$ in the transects T_{50} to T_{175}, without sign reversals. The three sigmoidal models are capable of fitting a portion of the sigmoid, demonstrating a monotonic decreasing behaviour ($R(t) \leq 0$), in the T_{50} t T_{175}, with no sign changing sections

(R(t) > 0), as observed in the QM. However, the SL3 model could not model elevated recession rates (|R(t)| > 0.35 m/y) effectively, often reverting to a quasi-linear trend, resembling the LM.

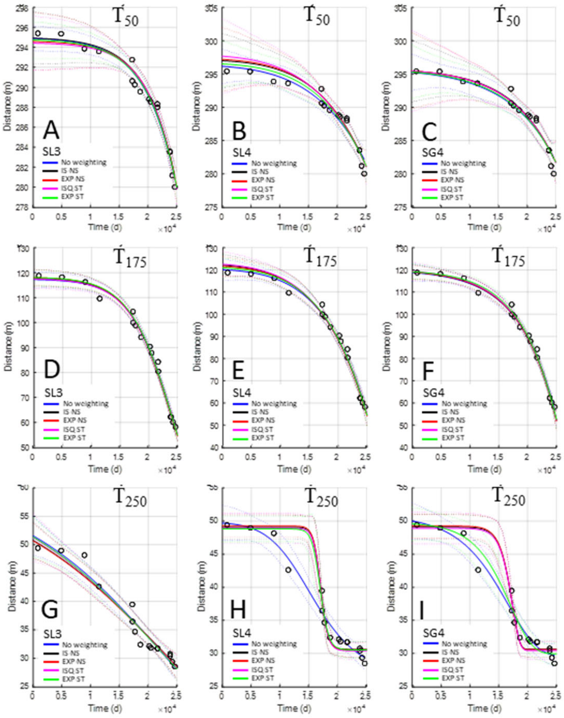

Figure 7. Sigmoidal regression results from SL3, SL4 and SG4 models to distance vs. time (days since FD56) at control transects 50, 175 and 250 (solid curves) with their 95% prediction intervals across the fit range (dotted curves around each sigmoidal model), applying the four weighting schemes considered in this work (Table 3) and without weighting.

Across the full set of transects, a generalised trend of increasing recession velocity (R(t) < 0) is observed over the course of the study, spanning all transects and years, in contrast to the QM model, which exhibits no time sections with R(t) > 0. The SL3 model produced three distinct spatial behaviours (Figure 8A, 8D, 8G): (1) western sector (T_1–T_{120}) with accelerating recession up to 1 m/y; (2) central sector (T_{120}–T_{220}) with acceleration exceeding 2.5 m/y; and (3) eastern sector (T_{220}–T_{294}) with nearly static trends (0.2–0.4 m/y). The SL3 model demonstrates no substantial disparities between the two standardised weighting schemes (ISQ-ST and EXP-ST, Figures 8D, 8G), even in the absence of any weighting (Figure 8A). Unlike SL3, both SL4 and SG4 models exhibit more complex behaviour, including transition bands, sensitive to the applied weighting.

From the western edge to T80 (≈400 m), recession accelerates to 0.7 m/y. Between T_{80} and T_{125}, an initial increase (up to 0.9 m/y) is followed by a slight deceleration to 0.3 m/y around 2000 y. Then, from T_{125} to T_{200}, the behaviour mirrors SL3 but over a shorter segment. Within this band, recession velocities can reach 5 m/y under the ISQ-ST weighting scheme. Between T_{200} and T_{240} (≈1100–1200 m), a narrow transition is detected, distinguishable only with weighting. The trend here is quasi-linear with $R(t)<0.5$ m/y. From T_{240} to T_{275} (≈1200–1500 m), an initial acceleration phase up to 3.5 m/y is followed by a post-2000 y deceleration down to 0.1 m/y in 2023 y. This decelerating sigmoidal behaviour is better captured with SL4 than SG4, which identifies only a narrow transition in this zone. The application of sigmoidal models is particularly sensitive to the weight attributed to historical datasets. In unweighted regressions, early image sources such as BAS79 and SAF86 overly influence the fit, distorting detection of inflection points. When uncertainty-based weighting is applied, the minimum in R(t)—corresponding to the sigmoid inflection—is consistently observed between $3.75–10^4$ and $4–10^4$ days (~2003–2005).

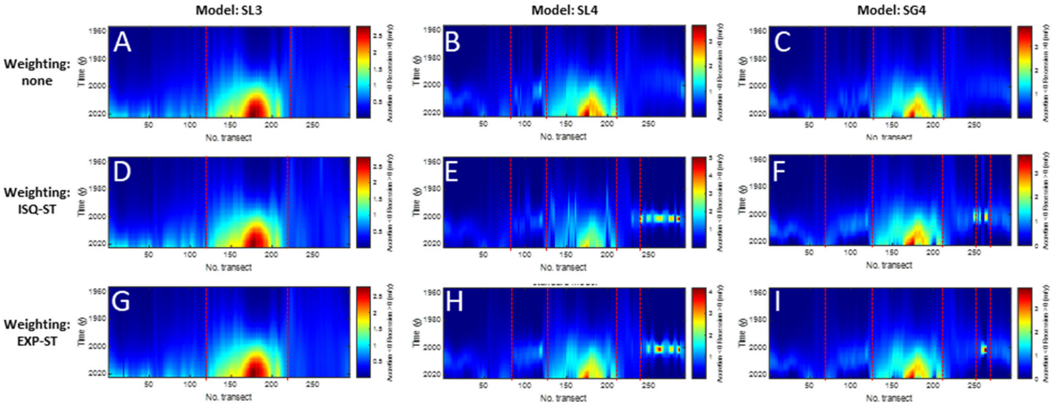

Figure 8. Instantaneous recession R(t) map (in m/y) fitted with the SL3, SL4 and SG4 (R(t) for each model in Table 4) along the time interval [1956, 2022] for each j^{th} transect (j=1..294) along the study area, first row R(t) maps without weighting, second row R(t) maps with weighting (ISQ-ST), and third row R(t) maps with weighting (EXP-ST). The detected change in R(t) dynamics, along the study area, is marked with red dashed lines on each map, see their explanation in the main text.

The comparative quality of the regression models was assessed via three diagnostics: standard error of the estimate, R^2, and corrected Akaike Information Criterion (AICc). The standard error (Figure 9A) increases markedly between 900 m and 1100 m across all models. The LM model shows the highest error, especially in this central region (STd about 2.0–2.67), with smaller errors in the western (0.31–0.96) and eastern (0.28–0.69) segments. The QM model maintains STd errors between 0.2–1.0, rarely exceeding 0.8 even in the problematic central section. For SL3, SL4 and SG4, standard errors rarely exceed 0.6 and remain below 0.4 with weighting. The estimation of the predictability quality, as indicated by R^2 (Figure 9B), varies across models. For LM, R2 ranges from 60% to 98%, depending on location. QM achieves over 90% for most transects, surpassing

https://doi.org/10.5194/egusphere-2025-3269
Preprint. Discussion started: 29 September 2025

95% with weighting. The sigmoidal models (SL3, SL4, SG4) consistently exceed 95% R2, largely unaffected by weighting. The corrected Akaike information index (AICc) at finite sample size behaviour (Figure 9C) mirrors that of standard error. For LM, AICc values vary from 14 to 50 (west), 12 to 41 (east), and reach 77–84 in the central section. The QM shows a rising AICc from 10 (west) to above 40 (central) before decreasing again. Sigmoidal models have consistently lower AICc than QM, reinforcing their suitability.

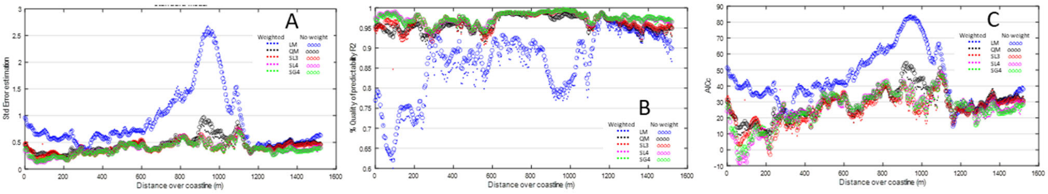

Figure 9. A) Standard error of estimation (STDE), B) R^2 or quality of predictability (in %), and C) Akaike information index corrected (AICc) for the models used in this work (Table 4) related with distance travelled along the coastline from western initial point.

6 Discussion

This study presents a robust, multidecadal spatial-temporal analysis of cliff recession at Port Foster, Deception Island, a geologically active sector of the South Shetlands, Antarctica. By integrating photogrammetric reconstructions from historical aerial and modern satellite images, it contributes a rare, high-resolution record of shoreline change spanning 1956 to 2023. Crucially, it reveals that recession dynamics at this periglacial site exhibit strong non-linearity, diverging significantly from the linear assumptions often employed in traditional Shoreline Change Analysis (SCA). The novelty of our approach lies in applying sigmoidal and quadratic regression models—rarely used in polar settings—demonstrating their suitability in environments characterised by episodic, threshold-based geomorphological responses. This work thus provides a much-needed Antarctic counterpoint to Arctic-dominated literature on coastal permafrost degradation and sets a methodological benchmark for future geomorphological monitoring in data-scarce regions.

Earlier research in Arctic and sub-Arctic permafrost coasts (e.g., Aga et al., 2024; Irrgang et al., 2018) has long acknowledged the inadequacy of linear models to capture episodic retreat driven by permafrost thaw and wave energy. Previous Antarctic shoreline studies have primarily focused on large scale coastal permafrost erosion (e.g., Tsiakos and Chalkias, 2023), with limited attention given to local periglacial cliff erosion processes. Our findings extend these insights to the Antarctic context, where cliff recession has received less systematic attention. To ensuring the reliability of SCS, accurate georeferencing and photogrammetric pre-processing were fundamental. In this study, the use of Structure-from-Motion Multi-View Stereo (SfM-MvS) processing facilitated the generation of high-resolution orthomosaics from historical aerial images, overcoming many of the challenges associated with working with legacy datasets. While Cook (2017) and Clark et al. (2023) demonstrated the effectiveness of Structure-from-Motion Multi-View Stereo (SfM-MvS) in modern coastal settings, our use of these techniques on legacy Antarctic datasets bridges a significant gap. Despite these improvements, the process still introduces some degree of positional uncertainty, particularly when working with lower-resolution images from earlier aerial surveys (e.g., 1956 FIDASE or 1968 SHNA flights). The root mean square error (RMSE) obtained for georeferenced datasets varied across image sources, with older datasets exhibiting greater discrepancies due to distortions and scale inconsistencies. While our methodology successfully minimized these errors using different weighting schemas, future studies could benefit from the integration of high-precision UAV or satellite altimetry datasets to further refine image alignment and reduce uncertainties.

Once the SCS was performed over the resulting point cloud from TBM, the observed non-linear erosion patterns at Port Foster contrast with earlier assumptions that Antarctic coastal change occurs at a slow and steady rate due to the region's colder climate and relatively lower energy marine environment (Sziło and Bialik, 2018; Hrbáček et al., 2023). Moreover, consistent with recent work by Tsai (2024) on non-linear erosion in Arctic coasts, we identify sigmoidal behaviours—initial stability, acceleration, and recent deceleration—in multiple transects. These results challenge recent Antarctic models such as those proposed by Philipp et al. (2022), which often assume uniform retreat across entire coastal sectors. Our findings support previous studies, but in the Arctic (e.g., Barnhart et al., 2014a and 2014b), that indicate periglacial coastal systems are increasingly vulnerable to climate change-induced erosion. This contradicts earlier studies that assumed a predominantly linear recession trend in Antarctic coastal bluffs, similar to those observed in temperate environments (Mishra et al., 2020). This suggests that bluff recession in this study zone is not a steady process but instead responds dynamically to external forcing (Jones et al., 2020; Philipp et al., 2022). The presence of an initial period of slow retreat followed by accelerated loss aligns with recent findings in Arctic studies, which highlight the role of increasing air and sea temperatures in weakening permafrost-affected sediments (Gibbs et al., 2021; Nielsen, 2022). The acceleration in erosion rates post-2001 observed in this study and the small-scale sectoring extracted (Figure 11) from results, suggests that Antarctic coastal bluffs and may in other Antarctic coastal areas, may be experiencing climate-induced changes at a faster rate than previously expected, potentially mirroring trends seen in the Arctic (Burningham and French, 2017; Pang et al., 2023). The use of non-linear statistical approaches in this study aligns with recent efforts in Arctic research to incorporate more sophisticated methodologies, such as machine learning-based Gaussian regression models and process-based modeling (Barnhart et al., 2014a; Islam and Lubbad, 2022). These advancements suggest that traditional linear regression models are becoming obsolete in polar coastal research, necessitating a shift towards non-linear and probabilistic approaches to accurately forecast future polar coastal changes.

https://doi.org/10.5194/egusphere-2025-3269
Preprint. Discussion started: 29 September 2025

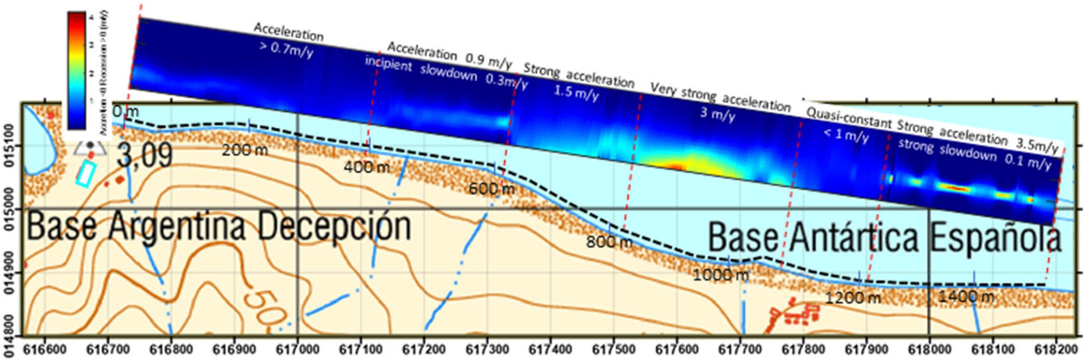

Figure 10. A) Standard error of estimation (STDE), B) R^2 or quality of predictability (in %), and C) Akaike information index corrected (AICc) for the models used in this work (Table 4) related with distance travelled along the coastline from western initial point.

From a theoretical perspective, the study contributes to understanding recession as a complex, multi-scalar process influenced by feedbacks between climatic, geological, and anthropogenic factors. The detected heterogeneity along the cliff—evidenced by three behaviour zones—supports a conceptual model in which recession rates are modulated by permafrost structure, topographic exposure, and human proximity. The high-resolution spatial pattern of Pearson's correlation coefficients (from −0.78 to −1.0) and the covariance values (approaching -140×10^3 in central zones) underscore the non-stationarity of recession forces. The alignment of maximum cliff instability with areas adjacent to infrastructure, such as the BAEGC, reinforces theoretical expectations about thermal perturbation effects of built environments on ground ice stability (Figure 10).

The implementation of the CREES Matlab-based tool, which integrates photogrammetric uncertainties directly into the regression analysis through weighting (via Equations 1 and 2), provides an open methodological framework that is transferable to other polar and high-latitude environments. Researchers working with fragmented or inconsistent datasets, particularly in settings with high logistical barriers, can adapt this weighted-least-squares approach to enhance model robustness. Moreover, our demonstration of improved predictive quality ($R^2 > 95\%$ for sigmoidal models) confirms the practical benefit of this refinement.

Given the observed acceleration and deceleration cycles in coastal retreat—especially evident between 2000 y and 2023 y—this study underscores the need for dynamic models in coastal geomorphology, capable of capturing time-varying responses to environmental forcings. As satellite archives expand and UAV deployments become more feasible in polar regions, the field is poised to shift from static assessments of coastal change to dynamic, process-based modelling. The future of Antarctic coastal research lies in combining such models with real-time environmental monitoring and thermal imaging to link atmospheric anomalies, permafrost degradation, and morphological change.

By demonstrating the value of long-term, high-resolution, uncertainty-weighted regression modelling, our study provides an improved analytical baseline for understanding cliff dynamics under climate stressors. The sigmoidal models (SL3, SL4, SG4), in particular, revealed recession peaks as high as 3.5 m/y (e.g., at T_{250}), followed by marked deceleration—features missed by both linear and polynomial fits. The standard error of the sigmoidal models remained consistently below 0.4 (with weighting), and AICc values outperformed those of linear and quadratic models across all zones, especially in the central 600–1100 m shoreline range.

Beyond academic advancement, the implications of this work extend to environmental management and policy. With several research bases situated within 200 m of retreating cliffs, a clear need arises for integrated erosion monitoring frameworks. Our model, validated across 294 transects, offers authorities a decision-support tool to identify risk-prone sectors and develop tailored protection strategies. The incorporation of spatially explicit uncertainty weighting is particularly valuable for producing credible early-warning signals in logistical planning for seasonal base activities. Therefore, this study advances the understanding of Antarctic periglacial coastal recession by: (i) demonstrating the failure of linear regression to adequately represent long-term shoreline evolution, (ii) validating sigmoidal models as superior alternatives for characterising episodic erosion, (iii) emphasising the importance of uncertainty-informed weighting in statistical coastal analyses, (iv) highlighting strong spatial heterogeneity in recession rates linked to local geomorphology and infrastructure, and (v) offering a transferable methodological framework for high-latitude cliff monitoring using legacy imagery.

Despite these contributions, the study has several limitations. First, the reliance on manual digitisation, while necessary due to low image contrast in some historical datasets, introduces subjectivity. Future work should explore semi-automated edge-detection algorithms (Swirad et al., 2021, 2022; Lu et al., 2024) to reduce operator bias. Second, while our temporal resolution is high for an Antarctic site, annual or seasonal imagery remains unavailable, limiting insights into intra-annual variability or responses to extreme events. Efforts should be made to integrate UAV photogrammetry and satellite altimetry in upcoming campaigns to refine temporal granularity.

Additionally, the study is geographically restricted to a 1.5 km segment. While representative, caution is warranted when extrapolating results to the broader South Shetlands or Antarctic Peninsula. Comparative studies across multiple Antarctic sites—and against Arctic analogues—could illuminate regional controls on recession heterogeneity. Finally, more detailed ground temperature and permafrost stratigraphy data would allow coupling of physical drivers with morphological responses, moving from correlative to process-based models.

7 Conclusions

This study addresses the pressing need to refine methodologies for understanding and predicting coastal erosion in periglacial environments, focusing on the volcanic bluffs of Port Foster, Deception Island. Through a comprehensive analysis of a 66-year time series derived from historical aerial photography and satellite imagery, this research demonstrates that coastal retreat in Antarctic settings is inherently non-linear. Periods of accelerated erosion, particularly post-2001 y, alternate with intervals of relative stability. Traditional linear models proved inadequate in capturing these dynamics, often underestimating recession rates and failing to represent episodic behaviour observed in the field.

In contrast, the application of sigmoidal logistic models yielded a significantly improved characterisation of threshold-driven transitions in cliff retreat. These models enabled the identification of inflection points in erosion rates and offered a more realistic approximation of the geomorphological processes at play. The integration of uncertainty-weighted regression further strengthened model robustness, mitigating biases associated with variable data quality across the historical image archive. This approach sets a precedent for future analyses in data-scarce polar environments, where heterogeneity in imagery is common.

Methodologically, the study underscores the value of combining structure-from-motion photogrammetry, orthorectification, and SCS-TBM analysis within a GIS framework. While positional uncertainties inherent in older datasets introduce some limitations, the consistent application of ground control points and robust statistical weighting ensures that detected shoreline changes reflect genuine geomorphological trends. The TBM-based approach, coupled with uncertainty analysis, offers a replicable and scalable strategy for long-term coastal monitoring.

Scientifically, the findings have far-reaching implications. The acceleration of cliff recession observed since the early 2000s aligns with broader climatic trends affecting the Antarctic Peninsula, including rising air and sea surface temperatures, diminishing sea ice cover, and increased wave activity. These factors exacerbate permafrost degradation, particularly in non-cohesive pyroclastic deposits, where thermal and hydro-mechanical processes interact. The study also highlights spatial heterogeneity in recession rates, driven by localised differences in permafrost composition and the presence of anthropogenic thermal inputs from nearby research infrastructure. Despite these trends, erosion rates in Port Foster remain lower than those in the Arctic, pointing to key differences in permafrost stability, sediment properties, and coastal energy regimes. Practically, the results underscore the need to integrate non-linear models into coastal risk assessments and infrastructure planning in Antarctica. The proximity of scientific installations to actively retreating cliffs amplifies the urgency for mitigation strategies grounded in accurate forecasts. The demonstrated utility of non-linear regression models suggests they should be incorporated into future coastal vulnerability assessments, both in the Antarctic and other permafrost-affected regions.

Looking ahead, future research should expand spatial and temporal datasets, integrate extreme weather event analysis, and explore inter-regional comparisons between Antarctic and Arctic coastal systems. Doing so will enhance predictive modelling capabilities and inform more resilient adaptation strategies for rapidly changing cryospheric environments.

Author contributions.

CPB and IS conceptualization, IS and CS data curation, CP and IS investigation and formal analysis, GIS mapping and Matlab visualization, and writing the manuscript draft version, CP methodology and CREES software programming, MAR and CP funding acquisition and project administration.

Competing interests. The contact author has declared that none of the authors has any competing interests.

Acknowledgements. The authors are grateful for the support received from the B.A.G.C. staff, the Antarctic Campaign Office (OCA) and the Logistics Division of the Army General Staff (DIVOPE), the Hydrographic Institute of the Navy (IHM), the Spanish Polar Committee (CPE) of the Ministry of Science and Innovation, the PAZ Science Programme of the INTA-CEIT Space Division, and the researchers of the Geological Hazards Division of the IGME. Artificial intelligence was used solely for syntax and grammar checking of the manuscript in English, which is not the authors' native language. No AI was used for generative purposes in the writing of the scientific content.

Financial support. This work has been developed within the Project "Auscultation of active processes on the slope and the cliff coast of the surroundings of the Spanish Antarctic Station Gabriel de Castilla" of the INTA – Spanish Army. It is financed by the Ministry of Defence (T.DES15002) and jointly developed with professors from the Universidad Politécnica de Madrid. SAR-PAZ images were financed by INTA-CEIT Announcement of Opportunity (PAZ Science Phase) 2019-2022. Sanchiz and I. Santalices was supported by the INTA-ET grant SEP27/21, and I. Santalices was supported by the UPM Department Cooperation Grants program for Scientific Research 2023-24.

References

Aga, J., Piermattei, L., Girod, L., Aalstad, K., Eiken, T., Kääb, A., and Westermann, S.: Acceleration of coastal-retreat rates for high-Arctic rock cliffs on Brøggerhalvøya, Svalbard, over the past decade. Earth Surface Dynamics, 12(5), 1049-1070, doi: 10.5194/esurf-12-1049-2024, 2024.

Agisoft LLC. Agisoft Metashape User Manual: Professional Edition, Version 2.1; Agisoft LLC: St. Petersburg, Russia, 2024; Available online: http://www.agisoft.com/ (last accessed: 4 November 2024).

Albuquerque, M., Espinoza, J., Teixeira, P., de Oliveira, A., Corrêa, I., and Calliari, L.: Erosion or coastal variability: An evaluation of the DSAS and the change polygon methods for the determination of erosive processes on sandy beaches. Journal of Coastal Research, (65), 1710-1714, doi: 10.2112/SI65-289.1, 2013.

Ali, T. A. New methods for positional quality assessment and change analysis of shoreline features. Doctoral dissertation, The Ohio State University, 156 pp, 2003.

Ankrah, J., Monteiro, A., and Madureira, H.: Bibliometric analysis of data sources and tools for shoreline change analysis and detection. Sustainability, 14(9), 4895, https://doi.org/10.3390/su14094895, 2022.

Antelo, B. J., Vidal, J., and Berrocoso, M.: Determination of the tide constituents at Livingston and Deception Islands (South Shetland Islands, Antarctica), using annual time series. Dyna, 82(191), 209-218, http://dx.doi.org/10.15446/dyna.v82n191.45207, 2015.

Antoniades, D., Giralt, S., Geyer, A., Alvarez-Valero, A.M., Pla-Rabes, S., Granados, I., Liu, E.J., Toro, M., Smellie, J.L. and Oliva, M.: The timing and widespread effects of the largest Holocene volcanic eruption in Antarctica. Scientific Reports, 8, 17279, https://doi.org/10.1038/s41598-018-35460-x, 2018.

ASTM: ASTM Standard D2487-00 Standard Classification of Soils for Engineering Purposes (Unified Soil ClassificationSystem). West Conshohocken, Pensilvania, Estados Unidos, 12 pp, 2000.

Balaji, R., Kumar, S.S., Misra, A.: Understanding the Effects of Seawall Construction Using a Combination of Analytical Modelling and Remote Sensing Techniques: Case Study of Fansa, Gujarat, India, vol. 8, (no. 3), SAGE Publications Sage UK, London, England, 153–160. http://dx.doi.org/10.1177/1759313117712180, 2017.

Bamber, J. L., Oppenheimer, M., Kopp, R. E., Aspinall, W. P., and Cooke, R. M.: Ice sheet contributions to future sea-level rise from structured expert judgment. Proceedings of the National Academy of Sciences, 116(23), 11195-11200, https://doi.org/10.1073/pnas.1817205116, 2019.

Barnhart, K. R., Anderson, R. S., Overeem, I., Wobus, C., Clow, G. D., and Urban, F. E.: Modeling erosion of ice-rich permafrost bluffs along the Alaskan Beaufort Sea coast. Journal of Geophysical Research: Earth Surface, 119(5), 1155-1179, https://doi.org/10.1002/2013JF002845, 2014a.

Barnhart, K. R., Overeem, I. and Anderson, R. S.: The effect of changing sea ice on the physical vulnerability of Arctic coasts. The Cryosphere 8, 1777–1799, doi:10.5194/tc-8-1777-2014, 2014b.

Belova, N., Ermolov, A., Novikova, A., Ogorodov, S., and Stanilovskaya, Y.: Dynamics of low-lying sandy coast of the Gydan peninsula, Kara Sea, Russia, based on multi-temporal remote sensing data. Remote Sensing, 15(1), 48, doi: 10.3390/rs15010048, 2022.

Boak, E. H., and Turner, I. L.: Shoreline definition and detection: a review. Journal of coastal research, 21(4), 688-703, doi: 10.2112/03-0071.1, 2005.

Bonilla, M. J. G., Muñoz, J. M. C., Vázquez, N. C., and Priego, C. H.: The Scientific Exploitation of PAZ mission: PAZ Ciencia objectives and status. Procedia Computer Science, 239, 2223-2227, https://doi.org/10.1016/j.procs.2024.06.412, 2024.

Brecher, H. H.: Photogrammetric maps of a volcanic eruption area, Deception Island, Antarctica. In Institute of Polar Studies Report; Research Foundation and the Institute of Polar Studies, The Ohio State University: Research foundation, Columbus, OH, USA; Volume 52, 19 pp, 1975.

Bronen, R., and Chapin III, F. S. Adaptive governance and institutional strategies for climate-induced community relocations in Alaska. Proceedings of the National Academy of Sciences, 110(23), 9320-9325, https://doi.org/10.1073/pnas.1210508110, 2013.

Brooks, S. M., and Spencer, T.: Temporal and spatial variations in recession rates and sediment release from soft rock cliffs, Suffolk coast, UK. Geomorphology, 124(1-2), 26-41, https://doi.org/10.1016/j.geomorph.2010.08.005, 2010.

Burningham, H., and Fernandez-Nunez, M.: Shoreline change analysis. Sandy Beach Morphodynamics. 439–460. http://dx.doi.org/10.1016/B978-0-08-102927-5.00019-9, 2020.

Burningham, H., and French, J.: Understanding coastal change using shoreline trend analysis supported by cluster-based segmentation. Geomorphology 282, 131–149. http://dx.doi.org/10.1016/J.GEOMORPH.2016.12.029, 2017.

Caballero, O. A.: Proyecto de estabilización de la Base Antártica Española Gabriel de Castilla (Isla Decepción, Antártida). MSc dissertation. ETSICCP, Universidad de Granada. 356 p, 2023.

https://doi.org/10.5194/egusphere-2025-3269
Preprint. Discussion started: 29 September 2025

Caselli, A., dos Santos Afonso, M., Risso, C., García, A. and Ortiz, R.: Caracterización geoquímica de los gases volcánicos de isla Decepción (Shetland del Sur, Antártida). Revista de la Asociación Geológica Argentina, 57(1): 69-79, 2002.

Child, S. F., Stearns, L. A., Girod, L., and Brecher, H. H.: Structure-from-motion photogrammetry of antarctic historical aerial photographs in conjunction with ground control derived from satellite data. Remote Sensing, 13(1), 21, https://doi.org/10.3390/rs13010021, 2021.

Clark, A., Moorman, B. J., and Whalen, D.: UAV-SfM and Geographic Object-Based Image Analysis for Measuring Multi-Temporal Planimetric and Volumetric Erosion of Arctic Coasts. Canadian Journal of Remote Sensing, 49(1), 2211679, https://doi.org/10.1080/07038992.2023.2211679, 2023.

Cook, K.L.: An Evaluation of the Effectiveness of Low-Cost UAVs and Structure from Motion for Geomorphic Change Detection. Geomorphology, 278, 195–208, https://doi.org/10.1016/j.geomorph.2016.11.009, 2017.

Danforth, W. W., and Thieler, E. R.: Digital Shoreline Analysis System (DSAS) user's guide; version 1.0, US Geological Survey, 92-355, 1992.

Davidson, M.: Forecasting coastal evolution on time-scales of days to decades. Coast. Eng. 103928, https://doi.org/10.1016/j.coastaleng.2021.103928, 2021.

de Pablo, M.A., Molina, A., Recio, C. and Ramos, M.: Estudio de la capa activa en relación al módulo principal de la Base "Gabriel de Castilla", Isla Decepción, Antártida. Departamento de Geología, Geografía y Medio Ambiente, Universidad de Alcalá, Madrid, 51 pp, 2015.

de Pablo, M.A., Molina, A., Recio, C., Ramos, M., Goyanes, G. and Ropero, M.A.: Análisis del estado de la capa activa en el emplazamiento de la base antártica española Gabriel de Castilla, Isla Decepción, Antártida. Boletín Geológico y Minero, 128 (1), 69-92, doi: 10.21701/bolgeomin.128.1.004, 2017.

de Pablo, M.A., Jiménez, J.J., Ramos, M., Prieto, M., Molina, A., Vieira, G., Hidalgo, M.A., Fernández, S., Recondo, C., Calleja, J.F., Peón, J.J., Corbea-Pérez, A., Maior, C.N., Morales, M., and Mora, C. (2020). Frozen ground and snow cover monitoring in Livingston and Deception islands, Antarctica: preliminary results of the 2015-2019 PERMASNOW project. Cuadernos Investig. Geogr. 46 (1), 187–222, https://doi.org/10.18172/cig.4381, 2020.

Dolan, R., Hayden, B., and Heywood, J.: A new photogrammetric method for determining shoreline erosion. Coastal Engineering, 2, 21–39. doi:10.1016/0378-3839(78)90003-0, 1978.

Dolan, R., Fenster, M. S., and Holme, S. J.: Temporal analysis of shoreline recession and accretion. Journal of coastal research, 723-744, https://www.jstor.org/stable/4297888, 1991.

ESA: Sentinel Application Platform SNAP version 12.0.0. Available online: https://step.esa.int/main/download/snap-download/, last accessed 25 June 2025, 2025.

Farquharson, L. M., Mann, D. H., Swanson, D. K., Jones, B. M., Buzard, R. M., and Jordan, J. W.: Temporal and spatial variability in coastline response to declining sea-ice in northwest Alaska. Marine Geology, 404, 71-83, https://doi.org/10.1016/j.margeo.2018.07.007, 2018.

Fenster, M. S., Dolan, R., and Elder, J. F.: A new method for predicting shoreline positions from historical data. Journal of Coastal Research, 147-171, https://www.jstor.org/stable/4298075, 1993.

Fenster, M. S., Dolan, R., and Morton, R. A.: Coastal storms and shoreline change: signal or noise?. Journal of Coastal Research, 714-720, https://www.jstor.org/stable/4300222, 2001.

Figueiredo, D., Dos Santos, A., Mateus, M., and Pinto, L.: Hydrodynamic modelling of Port Foster, Deception Island, Antarctica. Antarctic Science, 30(2), 115-124, doi:10.1017/S0954102017000463, 2018.

Fritz, M., Vonk, J.E., and Lantuit, H.: Collapsing arctic coastlines. Nature. Climate Change 7, 6–7, https://doi.org/10.1038/nclimate3188, 2017.

Genz, A. S., Fletcher, C. H., Dunn, R. A., Frazer, L. N., and Rooney, J. J.: The predictive accuracy of shoreline change rate methods and alongshore beach variation on Maui, Hawaii. Journal of Coastal Research, 23(1), 87-105, https://doi.org/10.2112/05-0521.1, 2007.

Gibbs, A. E., and Richmond, B. M.: National assessment of shoreline change—Summary statistics for updated vector shorelines and associated shoreline change data for the north coast of Alaska, US-Canadian border to Icy Cape, US Geological Survey, No. 2017-1107, 21 pp., https://doi.org/10.3133/ofr20171107, 2017.

Gibbs, A. E., Nolan, M., Richmond, B. M., Snyder, A. G., and Erikson, L. H.: Assessing patterns of annual change to permafrost bluffs along the North Slope coast of Alaska using high-resolution imagery and elevation models. Geomorphology, 336, 152-164, https://doi.org/10.1016/j.geomorph.2019.03.029, 2019.

Gibbs, A. E., Erikson, L. H., Jones, B. M., Richmond, B. M., and Engelstad, A. C.: Seven decades of coastal change at Barter Island, Alaska: exploring the importance of waves and temperature on erosion of coastal permafrost bluffs. Remote Sensing, 13(21), 4420, https://doi.org/10.3390/rs13214420, 2021.

Gilbert, E., and Holmes, C.: 2023's Antarctic sea ice extent is the lowest on record. Weather, 79(2), 46-51, https://doi.org/10.1002/wea.4518, 2024.

Girod, L., Nielsen, N. I., Couderette, F., Nuth, C., and Kääb, A.: Precise DEM extraction from Svalbard using 1936 high oblique imagery. Geoscientific Instrumentation, Methods and Data Systems, 7(4), 277-288, https://doi.org/10.5194/gi-7-277-2018.

Gómez-Pazo, A., Payo, A., Paz-Delgado, M. V., and Delgadillo-Calzadilla, M. A.: Open digital shoreline analysis system: ODSAS v1. 0. Journal of Marine Science and Engineering, 10(1), 26, https://doi.org/10.3390/jmse10010026, 2022.

González-Herrero, S., Navarro, F., Pertierra, L. R., Oliva, M., Dadic, R., Peck, L., and Lehning, M.: Southward migration of the zero-degree isotherm latitude over the Southern Ocean and the Antarctic Peninsula: Cryospheric, biotic and societal implications. Science of the Total Environment, 912, 168473, https://doi.org/10.1016/j.scitotenv.2023.168473, 2024.

González-Posadas, J. (2019). Relaciones entre los procesos geodinámicos modificadores de la costa en el entorno de la Base Antártica Española “Gabriel de Castilla”, Isla Decepción, Antártida. BSc dissertation, Universidad Politécnica de Madrid. 197 pp.

González-Posadas, J., Paredes, C., and Ropero, M. Á.: Ground deformation as a result of the foundation of a new module in the Spanish Antarctic Base Gabriel de Castilla, Deception Island, Antarctica. Boletin Geologico y Minero, 133(2), 95-121, https://doi.org/10.21701/bolgeomin/133.2/004, 2022.

Goyanes, G. A.: Control climático e interacciones permafrost-volcanismo, Isla Decepción, Antártida. PhD dissertation, Universidad de Buenos Aires. Facultad de Ciencias Exactas y Naturales, 318 pp, 2015.

Griggs, G., and Reguero, B.G.: Coastal adaptation to climate change and sea-level rise. Water 13 (16), 2151. http://dx.doi.org/10.3390/W13162151, 2021.

Hapke, C. J., Plant, N. G., Henderson, R. E., Schwab, W. C., and Nelson, T. R.: Decoupling processes and scales of shoreline morphodynamics. Marine Geology, 381, 42-53, https://doi.org/10.1016/j.margeo.2016.08.008, 2016.

Heo, J., Kim, J. H., and Kim, J. W.: A new methodology for measuring coastline recession using buffering and non-linear least squares estimation. International Journal of Geographical Information Science, 23(9), 1165-1177, https://doi.org/10.1080/13658810802035642, 2009.

Himmelstoss, E. A., FitzGerald, D. M., Rosen, P. S., and Allen, J. R.: Bluff evolution along coastal drumlins: Boston Harbor islands, Massachusetts. Journal of Coastal Research, 22(5), 1230-1240, https://doi.org/10.2112/06A-0005.1, 2006.

Himmelstoss, E. A., Henderson, R.E., Farris, A.S., Kratzmann, M.G., Bartlett, M.K., Ergul, A., McAndrews, J., Cibaj, R., Zichichi, J.L., and Thieler, E.R.: Digital Shoreline Analysis System version 6.0: U.S. Geological Survey software release, https://doi.org/10.5066/P13WIZ8M, 2024.

Hopfenblatt, J., Geyer, A., Aulinas, M., Álvarez-Valero, A. M., Sánchez, A. P., Giralt, S., and Smellie, J. L.: DecTephra: A new database of Deception Island's tephra record (Antarctica). Journal of Volcanology and Geothermal Research, 425, 107516, https://doi.org/10.1016/j.jvolgeores.2022.107516, 2022.

Howat, I. M., Porter, C., Smith, B. E., Noh, M. J., and Morin, P.: The reference elevation model of Antarctica. The Cryosphere, 13(2), 665-674, https://doi.org/10.5194/tc-13-665-2019, 2019.

Hrbáček, F., Oliva, M., Hansen, C., Balks, M., O'Neill, T. A., De Pablo, M. A., Ponti, S., Ramos, M., Vieira, G., Abramov, A., Pastíriková, L. K., Guglielmin, M., Goyanes, G., Francelino, M. R., Schaefer, C. and Lacelle, D.: Active layer and permafrost thermal regimes in the ice-free areas of Antarctica. Earth-Science Reviews, 242, 104458, https://doi.org/10.1016/j.earscirev.2023.104458, 2023.

Irrgang, A. M., Lantuit, H., Manson, G. K., Günther, F., Grosse, G., and Overduin, P. P.: Variability in rates of coastal change along the Yukon coast, 1951 to 2015. Journal of Geophysical Research: Earth Surface, 123(4), 779-800, https://doi.org/10.1002/2017JF004326, 2018.

Irrgang, A. M., Bendixen, M., Farquharson, L. M., Baranskaya, A. V., Erikson, L. H., Gibbs, A. E., Ogorodov, S. A., Overduin, P. P., Lantuit, H., Grigoriev, M. N., Jones, B. M. Drivers, dynamics and impacts of changing Arctic coasts. Nature Reviews Earth and Environment, 3(1), 39-54, https://doi.org/10.1038/s43017-021-00232-1, 2022.

Islam, M. A., and Lubbad, R.: A process-based model for arctic coastal erosion driven by thermodenudation and thermoabrasion combined and including nearshore morphodynamics. Journal of Marine Science and Engineering, 10(11), 1602, https://doi.org/10.3390/jmse10111602, 2022.

Jackson, C. W.: Quantitative Shoreline Change Analysis of An Inlet-Influenced Transgressive Barrier System: Figure Eight Island, North Carolina. Master of Science dissertation, University of North Carolina at Wilmington, 95 pp, 2004.

Jackson, C. W.: Spatio-temporal analysis of barrier island shoreline change: the Georgia coast, U.S.A. Doctoral dissertation University of Georgia, 296 pp, 2010.

Jackson, C.W., Jr.; Alexander, C.R.; Bush, D.M.: Application of the AMBUR R package for spatio-temporal analysis of shoreline change: Jekyll Island, Georgia, USA. Computers & Geosciences, 2012, 41, 199–207, https://doi.org/10.1016/j.cageo.2011.08.009, 2011.

Jones, B. M., Irrgang, A. M., Farquharson, L. M., Lantuit, H., Whalen, D., Ogorodov, S., Grigoriev, M., Tweedie, C., Gibbs, A. E., Strzelecki, M. C., Baranskaya, A., Belova, N., Sinitsyn, A., Kroon, A., Maslakov, A., Vieira, G., Grosse, G., Overduin, P., Nitze, I., Maio, C., Overbeck, J., Bendixen, M., Zagórski, P., Romanovsky, V. E.: Arctic Report Card 2020: Coastal Permafrost Erosion. NOAA ID 27897, 10 pp. DOI : https://doi.org/10.25923/e47w-dw52, 2020.

Jones, B. M., Hinkel, K. M., Arp, C. D., and Eisner, W. R.: Modern erosion rates and loss of coastal features and sites, Beaufort Sea coastline, Alaska. Arctic, 361-372, https://www.jstor.org/stable/40513223, 2008.

Kazhukalo, G., Novikova, A., Shabanova, N., Drugov, M., Myslenkov, S., Shabanov, P., Belova, N., and Ogorodov, S.: Coastal Dynamics at Kharasavey Key Site, Kara Sea, Based on Remote Sensing Data. Remote Sensing, 15(17), 4199, https://doi.org/10.3390/rs15174199, 2023.

King, J. and Turner, J.: Antarctic meteorology and climatology. Cambridge University Press, Cambridge, 409 pp, 1997.

Köppen, W.: Klassifikation der Klimate nach Temperatur, Niederschlag und Jahresablauf (Classification of climates according to temperature, precipitation and seasonal cycle). Petermanns Geographische Mitteilungen, 193-203, 1918.

Kupilik, M., Witmer, F.D.W., MacLeod, E.-A., Wang, C. and Ravens, T.: Gaussian Process Regression for Arctic Coastal Erosion Forecasting, IEEE Transactions on Geoscience and Remote Sensing, 57, 3, 1256-1264, doi: 10.1109/TGRS.2018.2865429, 2019

Lantuit, H., Overduin, P. P., Couture, N., Wetterich, S., Aré, F., Atkinson, D., Brown, J., Cherkashov, G., Drozdov, D., Forbes, D.L., Graves-Gaylord, A., Grigoriev, M., Hubberten, H.W., Jordan, J., Jorgenson, T., 0degârd, R.S., Ogorodov, S., Pollard, W.H., Rachold, W., Sedenko, S., Solomon, S., Steenhuisen, F., Streletskaya, I., and Vasiliev, A.: The Arctic coastal dynamics database: A new classification scheme and statistics on Arctic permafrost coastlines. Estuaries and Coasts, 35, 383-400, https://doi.org/10.1007/s12237-010-9362-6, 2012.

Li, R., Liu, J. K., and Felus, Y.: Spatial modeling and analysis for shoreline change detection and coastal erosion monitoring. Marine Geodesy, 24(1), 1-12, https://doi.org/10.1080/01490410121502, 2001.

Li, W., Yan, D., Weng, B., and Zhu, L.: Research progress on hydrological effects of permafrost degradation in the Northern Hemisphere. Geoderma, 438, 116629, https://doi.org/10.1016/j.geoderma.2023.116629, 2023.

Liew, M., Xiao, M., Farquharson, L., Nicolsky, D., Jensen, A., Romanovsky, V., Peirce, J., Alessa, L., McComb, C., Zhang, X., Jones, B.: Understanding effects of permafrost degradation and coastal erosion on civil infrastructure in Arctic coastal villages: a community survey and knowledge co-production. Journal of Marine Science and Engineering, 10(3), 422, https://doi.org/10.3390/jmse10030422, 2022.

Limber, P. W., Barnard, P. L., Vitousek, S., and Erikson, L. H.: A model ensemble for projecting multidecadal coastal cliff retreat during the 21st century. Journal of Geophysical Research: Earth Surface, 123(7), 1566-1589, https://doi.org/10.1029/2017JF004401, 2018.

López-Martínez, J., Serrano, E., Schmid, T., Mink, S., and Lines, C.: Periglacial processes and landforms in the South Shetland Islands (northern Antarctic Peninsula region), Geomorphology, 155, 62–79, https://doi.org/10.1016/j.geomorph.2011.12.018, 2012.

Lu, Z. S., Wang, Y., Liang, S. Y., and Li, Z. C.: Automatic regionalized coastline extraction method based on high-resolution images. IEEE Access, 12, 13537-13552, doi: 10.1109/ACCESS.2024.3356710, 2024.

Martí, J., Geyer, A., and Aguirre-Diaz, G.: Origin and evolution of the Deception Island caldera (South Shetland Islands, Antarctica). Bulletin of Volcanology, 75(6), 1-18, https://doi.org/10.1007/s00445-013-0732-3, 2013.

Matsumoto, H., Dickson, M. E., Stephenson, W. J., Thompson, C. F., and Young, A. P.: Modeling future cliff-front waves during sea level rise and implications for coastal cliff retreat rates. Scientific Reports, 14(1), 7810, https://doi.org/10.1038/s41598-024-57923-0, 2024.

Mishra, M., Sudarsan, D., Kar, D., Naik, A. K., Das, P. P., Santos, C. A., and da Silva, R. M.: The development and research trend of using DSAS tool for shoreline change analysis: a scientometric analysis. Journal of Urban and Environmental Engineering, 14(1), 69-77, doi: 10.4090/juee.2020.v14n1.069077, 2020.

Mott, P.G.: Wings over Ice: The Falkland Islands and Dependencies Aerial Survey Expedition; Peter Mott: Long Sutton, UK, 167 pp, 1986.

Nguyen, L. D., Minh, N. T., Thy, P. T. M., Phung, H. P., and Huan, H. V.: Analysis of changes in the riverbanks of Mekong river-Vietnam by using multi-temporal remote sensing data. International Archives of the Photogrammetry, Remote Sensing and Spatial Information Science, 38(Part 8), 287-292, 2010.

Nicholls, R. J., and Cazenave, A.: Sea-level rise and its impact on coastal zones. science, 328(5985), 1517-1520, https://doi.org/10.1126/science.1185782, 2010.

Nielsen, D. M., Pieper, P., Barkhordarian, A., Overduin, P., Ilyina, T., Brovkin, V., Baehr, J., and Dobrynin, M.: Increase in Arctic coastal erosion and its sensitivity to warming in the twenty-first century. Nature Climate Change, 12(3), 263-270, https://doi.org/10.1038/s41558-022-01281-0, 2022.

North, R., and Barrows, T. T.: High-resolution elevation models of Larsen B glaciers extracted from 1960s imagery. Scientific Reports, 14(1), 14536, https://doi.org/10.1038/s41598-024-65081-6, 2024.

Over, J.R., Ritchie, A.C., Kranenburg, C.J., Brown, J.A., Buscombe, D., Noble, T., Sherwood, C.R., Warrick, J.A., and Wernette, P.A.: Processing coastal imagery with Agisoft Metashape Professional Edition, version 1.6—Structure from motion workflow documentation: U.S. Geological Survey Open-File Report 2021–1039, 46 p., https://doi.org/10.3133/ofr20211039, 2021.

Pang, T., Wang, X., Nawaz, R. A., Keefe, G., and Adekanmbi, T. (2023). Coastal erosion and climate change: A review on coastal-change process and modeling. Ambio, 52(12), 2034-2052.

Paredes, C., la Vega-Panizo, D., and Ropero, M.: Application of improved accuracy SFM-MVS for photogrammetric restitution and comparison of pre-and posteruption archival aerial imagery on Deception Island (South Shetland, Antarctica). In Proceedings 3rd Congress in Geomatics Engineering, Editorial Universitat Politècnica de València, 15-25, https://dx.doi.org/10.4995/CiGeo2021.2021.12755, 2021.

Peel, M., Finlayson, B. and McMahon, T.: Updated world map of the Köppen–Geiger climate classification. Hydrology and Earth System Sciences, 11, 1633-1644, https://doi.org/10.5194/hess-11-1633-2007, 2007.

Petropoulos, G. P., Petsini, T., and Detsikas, S. E.: Geoinformation Technology in Support of Arctic Coastal Properties Characterization: State of the Art, Challenges, and Future Outlook. Land, 13(6), 776, https://doi.org/10.3390/land13060776, 2024.

Philipp, M., Dietz, A., Ullmann, T., and Kuenzer, C.: Automated extraction of annual erosion rates for Arctic permafrost coasts using Sentinel-1, deep learning, and change vector analysis. Remote Sensing, 14(15), 3656, https://doi.org/10.3390/rs14153656, 2022.

Prates, G., and Vieira, G.: Surface Displacement of Hurd Rock Glacier from 1956 to 2019 from Historical Aerial Frames and Satellite Imagery (Livingston Island, Antarctic Peninsula). Remote Sensing, 15(14), 3685, https://doi.org/10.3390/rs15143685, 2023.

Prates, G., Torrecillas, C., Berrocoso, M., Goyanes, G., and Vieira, G.: Deception Island 1967–1970 Volcano Eruptions from Historical Aerial Frames and Satellite Imagery (Antarctic Peninsula). Remote Sensing, 15(8), 2052, https://doi.org/10.3390/rs15082052, 2023.

Prémaillon, M., Regard, V., Dewez, T. J., and Auda, Y.: GlobR2C2 (Global Recession Rates of Coastal Cliffs): a global relational database to investigate coastal rocky cliff erosion rate variations. Earth Surface Dynamics, 6(3), 651-668, https://doi.org/10.5194/esurf-6-651-2018, 2018.

Prieto-Ballesteros, O., Gómez, F., Moreno, M., de Diego, G., Fernandez-Sampedro, M., Martín-Redondo, M. P., and Parro, V.: Underground warmed environments at cold regions. The case of Cerro Caliente in Deception island, Antarctica. In European Planetary Science Congress, EPSC2012-466, 2012.

Ramos, M., Vieira, G., de Pablo, M.A., Molina, A., Abramov, A., and Goyanes, G.: Recent shallowing of the thaw depth at Crater Lake, Deception Island, Antarctica (2006–2014). Catena 149 (2), 519–528, https://doi.org/10.1016/j.catena.2016.07.019, 2017.

Rantanen, M., Karpechko, A. Y., Lipponen, A., Nordling, K., Hyvärinen, O., Ruosteenoja, K., Vihma, T., and Laaksonen, A.: The Arctic has warmed nearly four times faster than the globe since 1979. Communications earth and environment, 3(1), 168, https://doi.org/10.1038/s43247-022-00498-3, 2022.

Ravens, T. M., Jones, B. M., Zhang, J., Arp, C. D., and Schmutz, J. A.: Process-based coastal erosion modeling for drew point, North Slope, Alaska. Journal of Waterway, Port, Coastal, and Ocean Engineering, 138(2), 122-130, https://doi.org/10.1061/(ASCE)WW.1943-5460.0000106, 2012.

Riquelme, A., Del Soldato, M., Tomás, R., Cano, M., Bordehore, L. J., and Moretti, S. (2019). Digital landform reconstruction using old and recent open access digital aerial photos. Geomorphology, 329, 206-223, https://doi.org/10.1016/j.geomorph.2019.01.003, 2019.

Roland, T.P., Bartlett, O.T., Charman, D.J., Anderson, K., Hodson, K.A., Amesbury, M.J., Maclean, I., Fretwell, P.T., and

Rousseeuw, P. J., and Leroy, A. M.: Robust regression and outlier detection. John Wiley and Sons. 330 pp, 2003.

Ruggiero, P., Kratzmann, M.G., Himmelstoss, E.A., Reid, D.A.J., Kaminsky, G.: National assessment of shoreline change: historical shoreline change along the Pacific Northwest coast. US Geological Survey Open-File Report 2012-1007, 62 pp, https://doi.org/10.3133/ofr20121007, 2013.

Sam, S. C., and Gurugnanam, B.: Coastal transgression and regression from 1980 to 2020 and shoreline forecasting for 2030 and 2040, using DSAS along the southern coastal tip of Peninsular India. Geodesy and Geodynamics, 13(6), 585-594, https://doi.org/10.1016/j.geog.2022.04.004, 2022.

Scala, P., Manno, G., and Ciraolo, G.: Semantic segmentation of coastal aerial/satellite images using deep learning techniques: An application to coastline detection. Computers and Geosciences, 192, 105704, https://doi.org/10.1016/j.cageo.2024.105704, 2024.

Schoonees, T., Gijón Mancheño, A., Scheres, B., Bouma, T. J., Silva, R., Schlurmann, T., and Schüttrumpf, H.: Hard structures for coastal protection, towards greener designs. Estuaries and Coasts, 42, 1709-1729, https://doi.org/10.1007/s12237-019-00551-z, 2019.

Small D., and Schubert A.: Guide to S1 Geocoding, UZH-S1-GC-AD, Technical Note, Issue 1.10, 26.03.2019, 42 pp, https://sentinel.esa.int, 2019.

Smellie, J.L.: Geology. In López-Martínez, J., Smellie, J.L., Thomson, J.W. and Thomson, M.R.A. Eds. Geology and geomorphology of Deception Island, 11-30. BAS Geomap Series, 6-A. and 6–B, pp. 11–30. Cambridge: British Antarctic Survey, 77 pp, https://nora.nerc.ac.uk/id/eprint/17439, 2002.

Srivastava, A.: A least-squares approach to improved shoreline modelling. Doctoral dissertation, Ohio State University, 97 pp, 2005.

Streletskiy, D.: Permafrost degradation. In Haeberli, W. and Whiteman, C. (Eds.) Snow and Ice-Related Hazards, Risks, and Disasters. 2nd ed, Elsevier, 297-322, https://doi.org/10.1016/B978-0-12-394849-6.00010-X, 2021.

Sun, X., Lv, T., Sun, Q., Ding, Z., Shen, H., Gao, Y., He, Y., Fu, M., and Li, C.: Analysis of Spatiotemporal Variations and Influencing Factors of Sea Ice Extent in the Arctic and Antarctic. Remote Sensing, 15(23), 5563, https://doi.org/10.3390/rs15235563, 2023.

Sunamura, T.: Geomorphology of rocky coasts (Vol. 3). Chichester, Wiley, 302 pp, 1992.

Sunamura, T.: Rocky coast processes: with special reference to the recession of soft rock cliffs. Proceedings of the Japan Academy, Series B, 91(9), 481-500, https://doi.org/10.2183/pjab.91.481, 2015.

Swirad, Z. M., and Young, A. P.: Automating coastal cliff erosion measurements from large-area LiDAR datasets in California, USA. Geomorphology, 389, 107799, https://doi.org/10.1016/j.geomorph.2021.107799, 2021.

Swirad, Z. M., and Young, A. P.: CliffDelineaTool v1. 2.0: an algorithm for identifying coastal cliff base and top positions. Geoscientific Model Development, 15(4), 1499-1512, https://doi.org/10.5194/gmd-15-1499-2022, 2022.

Sziło, J., and Bialik, R. J.: Recession and ice surface elevation changes of Baranowski Glacier and its impact on proglacial relief (King George Island, West Antarctica). Geosciences, 8(10), 355, https://doi.org/10.3390/geosciences8100355, 2018.

Tanner, W.F.: Standards for Measuring Shoreline Change. Department of Geology, Florida State University, Tallahassee, Florida, 87 pp., 1978.

Torrecillas, C., Zarzuelo, C., de la Fuente, J., Jigena-Antelo, B., and Prates, G.: Evaluation and Modelling of the Coastal Geomorphological Changes of Deception Island since the 1970 Eruption and Its Involvement in Research Activity. Remote Sensing, 16(3), 512, https://doi.org/10.3390/rs16030512, 2024.

Trenhaile, A. S.: Predicting the response of hard and soft rock coasts to changes in sea level and wave height. Climatic Change, 109(3), 599-615, https://doi.org/10.1007/s10584-011-0035-7, 2011.

Tsai, Y. L. S.: Monitoring Arctic permafrost coastal erosion dynamics using a multidecadal cross-mission SAR dataset along an Alaskan Beaufort Sea coastline. Science of the Total Environment, 917, 170389, https://doi.org/10.1016/j.scitotenv.2024.170389, 2024.

Tsiakos, C. A. D., and Chalkias, C.: Use of machine learning and remote sensing techniques for shoreline monitoring: A review of recent literature. Applied Sciences, 13(5), 3268, https://doi.org/10.3390/app13053268, 2023.

Turner, J., Barrand, N. E., Bracegirdle, T. J., Convey, P., Hodgson, D. A., Jarvis, M., Jerkins, A., Marshall, G., Meredith, M.P., Roscoe, H., Shanklin, J., French, J., Goose, H., Guglielmin, M., Gutt, J., Jacobs, S., Kennicutt II, M.C., Masson-Delmotte, V., Mayewski, P., Navarro, F., Robinson, S., Scambos, T., Sparrow, M., Summerhayes, C., Speer, K., and Klepikov, A.: Antarctic climate change and the environment: an update. Polar Record, 50(3), 237–259, doi:10.1017/S0032247413000296, 2014.

Vidal, J., Berrocoso, M., and Fernández-Ros, A.: Study of tides and sea levels at Deception and Livingston islands, Antarctica. Antarctic Science, 24(2), 193-201, doi:10.1017/S095410201100068X, 2012.

Vieira, G., López-Martinez, J., Serrano, E., Ramos, M., Gruber, S., Hauck, C. and Blanco, J.J.: Geomorphological observations of permafrost and ground-ice degradation on Deception and Livingston Islands, Maritime Antarctica. 9th International Conference on Permafrost, Fairbanks, Alaska, Extended Abstracts, Vol. 1, Kane D, Hinkel K (eds). University of Alaska Press: Fairbanks; 1839–1844, https://doi.org/10.5167/uzh-3320, 2008.

Vukadinov, D., Jovanovic, R., and Tuba, M. I. L. A. N.: An algorithm for coastline extraction from satellite imagery. Int. J. Comput., 2, 8-15, 2017.

Wang, Z., Xiao, M., Nicolsky, D., Romanovsky, V., McComb, C., and Farquharson, L.: Arctic coastal hazard assessment considering permafrost thaw subsidence, coastal erosion, and flooding. Environmental Research Letters, 18(10), 104003, doi: 10.1088/1748-9326/acf4ac, 2023.

Warnasuriya, T. W. S., Kumara, M. P., Gunasekara, S. S., Gunaalan, K., and Jayathilaka, R. M. R. M.: An improved method to detect shoreline changes in small-scale beaches using Google Earth Pro. Marine Geodesy, 43(6), 541-572, https://doi.org/10.1080/01490419.2020.1822478, 2020.

Warnasuriya, T.W.S.: Assessing the influence of transect interval in monitoring and analysis of shoreline change. Environ Monit Assess 195, 532, https://doi.org/10.1007/s10661-023-11161-5, 2023.

Young, A.P., Flick, R.E., Gutierrez, R. and Guza, R.T.: Comparison of short-term seacliff retreat measurement methods in Del Mar, California. Geomorphology, 112, 318–323, https://doi.org/10.1016/j.geomorph.2009.06.018, 2009.

Young, A. P., and Carilli, J. E.: Global distribution of coastal cliffs. Earth Surface Processes and Landforms, 44(6), 1309-1316, https://doi.org/10.1002/esp.4574, 2019.

Zarillo, G. A., Kelley, J., and Larson, V.: A GIS based tool for extracting shoreline positions from aerial imagery (BeachTools) revised. Coastal and Hydraulics Laboratory Engineering Technical Note ERDC/CHL CHETN-IV-73, Vicksburg, MS: U.S. Army Engineer Research and Development Center, 14 pp., http://chl.erdc.usace.army.mil/chetn, 2008.

Ziaja, W., Ostafin, K., Maciejowski, W., and Kruse, F.: Coastal landscape degradation and disappearance of Davislaguna Lake, Sørkappland, Svalbard, 1900–2021. Land Degradation and Development, 34(16), 4823-4832, https://doi.org/10.1002/ldr.4765, 2023.